Schedule for Presentation Meeting of Master-Degree Thesis in 2018
International Course of Maritime & Urban Engineering

Date :   August 1st (Wednesday) starting from 09:30

Venue :   S1-312   Lecture Room

No.	Time	Name	Supervisor	Title of thesis	Chairman
1	09:30 – 09:55	PRADHAN Sujan	Sanada	Seismic Performance Evaluation of RC Beam Considering Buckling of Longitudinal Reinforcing Bar	Iijima
2	09:55 – 10:20	ROYCHOUDHURY Seemontini	Toda	CFD Study on KCS Maneuvering in Calm Water	Iijima
3	10:20 – 10:45	KHOIRI Putika Ashfar	Nishida/Irie	Parameter Estimation of a Distributed Hydrological Model in the Ibo River Basin Using the Polynomial Chaos Expansion Method	Iijima
4	10:45 – 11:10	Thant Zin Htun	Suzuki	Motion Analysis of ROV Coupled With Tether	Iijima
5	11:10 – 11:35	Myo Zin Aung	Umeda	Minimum Propulsion Power Prediction of a Ship under Adverse Weather Conditions with Dynamics of Diesel Engine and Turbocharger Taken into Account	Iijima
				Lunch Break	
6	13:00 – 13:25	ADILAH Ahmad	Iijima	Structural Analysis of a Floating Vertical Axis Wind Turbine	Suzuki
7	13:25 – 13:50	ZHOU Dali	Kashiwagi	Numerical Calculation of Ship Hydroelasticity Using Enhanced Unified Theory	Suzuki
8	13:50 – 14:15	Aung Kyaw Htet	Fujikubo	Ultimate Strength of a Continuous Stiffened Panel under Combined Transverse Thrust and In-plane Shear	Suzuki
				Break	
9	14:30 – 14:55	AMRA Rajuli	Aoki	Adaptive Mitigation Approach for Tsunami Ascending to Meandering River	Irie
10	14:55 – 15:20	MWANGI Benson Oyunge	Toda	SPIV (Stereo-Particle Image Velocimetry) Measurement for a Self-propelled Ship in Regular Head Waves with Different	Irie
11	15:20 – 15:45	KRISTOV Ivan William	Osawa	Verification and Validation of a Cellular Automaton Simulating Under-Film Corrosion	Irie
	16:00 –	at S1-323 Meeting for Evaluating Mater-thesis Presentations, and Steering Committee Meeting			

Meeting for Evaluation: From 16:00 at S1-323 Meeting Room

Members are Steering committee members and the supervisors

Seismic Performance Evaluation of RC Beam Considering Buckling of Longitudinal Reinforcing Bar

Sujan Pradhan

Concrete Structure Laboratory, Department of Architecture Engineering

Key Words: *Full scale test, Performance based design, Reinforced concrete, Safety limit, Seismic assessment*

1. Introduction

The strong column-weak beam type frame structures possess better energy dissipation capacity during the earthquake. Hence, based on the performance based seismic design, strong column-weak beam type RC moment resistant frame structures are effectively used. The safety limit of RC beam members applied to the seismic performance evaluation of RC buildings [1] is defined as the smallest of drift ratios at which (1) the flexural resistance decreases to 80% of its maximum strength, (2) shear failure occurs after flexural yielding and (3) tensile rupture of beam longitudinal reinforcement bar occurs.

However, in a series of static loading experiment of strong column-weak beam type RC frames [2], damage conditions defined as above (from (1) to (3)) were not observed even under large drifts, but the buckling phenomena of the beam longitudinal bars were visually observed after the cover concrete was peeled off at the beam ends. This experiment showed that the reduction in strength due to the buckling was related to the safety limit of strong column-weak beam type RC moment-resisting buildings.

Many studies have focused on the buckling of longitudinal reinforcing bars in columns under high axial forces. However, limited studies focused that in beams. Hence, the method to estimate the buckling occurrence point for beam longitudinal reinforcing bars had been proposed in past research [3]. In the current research, the buckling of beam longitudinal reinforcing bars observed in the previous experiment [2] was experimentally re-examined and the applicability of the proposed evaluation method [3] was verified using full scale beam specimens, as the previous research [2] tested small scaled frame specimens with common beam structural details and the evaluation method [3] was applied to only one common type of beam.

2. Experiments on Full Scale Beam Specimens Focusing on Buckling of Longitudinal Reinforcing Bars

2.1 Specimens and loading system

Three full scale beam specimens were designed based on the beams in the scaled specimen, each with height of 1540 mm and cross-section of 450 X 700 mm. They had different diameters of longitudinal reinforcing bars and spacing of shear reinforcing bars, as shown in Table 1, which were likely to affect bucking of beam longitudinal bars.

The specimens were tested using the static loading system at Osaka University. Every specimen was subjected to a constant axial load of $N/N_0 = 0.07$ (where N is the axial load, and N_0 is the compressive strength of the specimen). The axial load was applied to the beam specimens, as the previous experiment [2] reported that the axial load of 7% to the beam compressive

strength was induced due to the restriction to beam elongation by the columns. Equation (1) gives the axial forces for the south (N_S) and north (N_N) vertical jacks during the experiment to maintain a bending moment diagram representing that in the previous beam member [2], as shown in Fig. 1.

Table 1 Specifications of the specimens

Descriptions	Specimen1	Specimen 2	Specimen 3
Longitudinal bar	6-D25	10-D19	6-D25
Shear reinforcing bars	D13@200	D13@200	D10@100

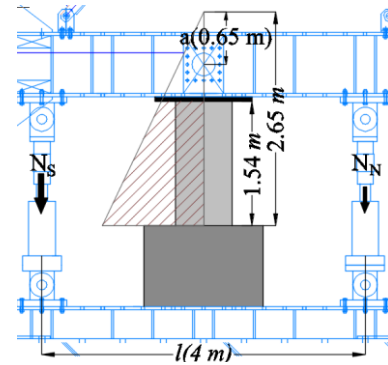$$N_S = N/2 + Q. \, a/l$$
$$N_N = N/2 - Q. \, a/l$$
(1)

Fig.1 Target bending moment

2.2 Experimental results

Fig. 2 shows the comparison of beam shear force vs. experimental drift ratio relationships. Flexural cracks occurred at each beam end during the first cycle to $R = 0.55\%$ rad, and every specimen formed a yield mechanism after flexural yielding at the critical section. Thus, the stiffness degraded in the following cycles. However, the shear resistance still increased with an increase of drift before the buckling of longitudinal reinforcing bars.

The vertical compression cracks along the longitudinal reinforcing bars on each specimen appeared during the negative cycle to $R = 2.18\%$ rad, as well as the flexural resistance decreased during the next cycle to $R = 3.30\%$ rad, which indicated that the buckling of longitudinal reinforcing bars in each specimen was initiated from the cycle to $R = 2.18\%$ rad.

Comparing specimens 1 and 2, the shear reinforcing bar spacing was the same but the diameter of longitudinal reinforcing bars was different. The shear resistance was significantly decreased for specimen 2 with the smaller diameter of longitudinal reinforcing bar, whereas it was a little moderate for specimen 1 after the initiation of longitudinal reinforcing bar buckling.
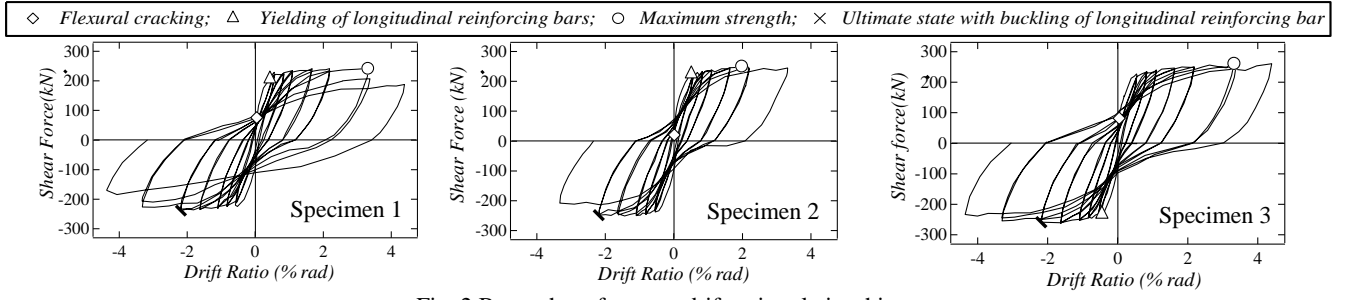
Fig. 2 Beam shear force vs. drift ratio relationships

Comparing specimens 1 and 3, the diameter of longitudinal reinforcing bars was the same but the shear reinforcing bar spacing was different. The shear resistance was dropped significantly for specimen 1 with larger shear reinforcing bar spacing, whereas it was little moderate for specimen 3 after the buckling of longitudinal reinforcing bar.

During the static loading experiments, the tensile force pulled out the longitudinal reinforcing bars from the stub, which affected the experimentally measured drift. To obtain the pull-out length, strains of longitudinal reinforcing bars at different depth were monitored by strain gauges. However, the strain gauge data was found to be reliable only for specimen 1. Hence, in this research, the flexural drift ratio was evaluated excluding the pull-out behavior and comparison of experimental and analytical drift at the buckling of the longitudinal reinforcing bar was performed only for specimen 1. After modifying the flexural drift without pull-out behavior (R_n), the buckling of longitudinal reinforcing bars of specimen 1 was found to be initiated during the cycle to R_n = 1.52% rad., as shown in Fig. 3.

3. Analytical Evaluation for Drift at Buckling of Beam Longitudinal Reinforcing Bars

3.1 Cyclic cross-section analysis

To investigate the stress-strain behavior of longitudinal reinforcing bars to evaluate the drift at its buckling during the cyclic loading, the cyclic cross-section analysis was performed by fiber approach. Trilinear model and Menegotto Pinto steel model were used for concrete and reinforcing bars, respectively. The relation between the drift ratio and the curvature was evaluated assuming deflection characteristics of the beam specimen to perform the analysis with the curvature equivalent to the experimental drift without pull-out behavior and the stress-strain behaviors of longitudinal reinforcing bars were investigated.

3.2 Estimation for longitudinal reinforcing bars buckling

The estimation of longitudinal reinforcing bars buckling drift was based on the previous evaluation method [3]. The buckling resistance strength (σ_E) of longitudinal reinforcing bars was obtained by using the equation (2).

$$\sigma_E = \frac{4 \times \pi^2 \times I}{L_B^2 \times A_r} \times E_r \qquad (2)$$

where, I and A_r are the moment of inertia and the cross-sectional area of longitudinal reinforcing bar; L_B is the center to center spacing of shear reinforcing bars and E_r is equivalent stiffness coefficient.

The value of equivalent stiffness coefficient was evaluated based on the method used by Akiyama et. al.[4]. The buckling resistance strength (σ_E) was calculated at every point of the investigated stress-strain curve of longitudinal reinforcing bar and then compared with respective working stress. The buckling resistance strength (σ_E) became less than the working stress during the cycle to R_n = 1.52% rad. Hence, the beam longitudinal reinforcing bars buckling drift for specimen 1 was estimated to be R_n = 1.52% rad. Fig. 3 shows the experimental and analytical shear force and drift ratio (without pull-out behavior) relationship with experimental and analytical buckling drifts. This shows that the drift at beam longitudinal reinforcing buckling from the analysis had a good agreement with that from the experiment.
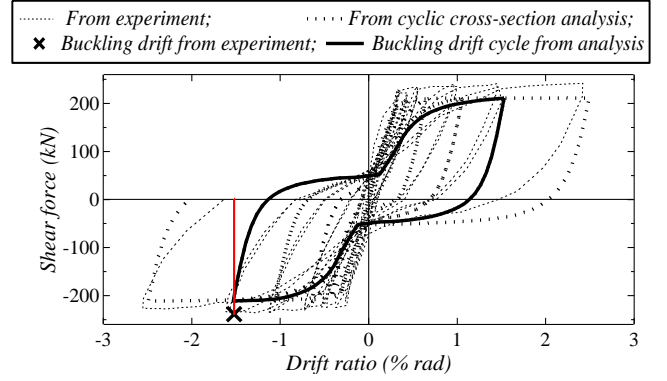
Fig.3 Comparison of the drifts at bucking from the experiment and analysis

4. Conclusions

1. The buckling of beam longitudinal reinforcing bars observed in the previous study was experimentally verified in full scale beam specimens.
2. Buckling initiation drift was found to be independent to the diameter of longitudinal reinforcing bars and the spacing of shear reinforcing bars within this series of tests.
3. The diameter of longitudinal reinforcing bars and the spacing of shear reinforcing bars affected the drop in shear resistance of RC beam after the buckling of longitudinal reinforcing bar.
4. The evaluation method for beam longitudinal reinforcing bar buckling proposed in the past research was found to be applicable to full scale beam members.

References

1) AIJ: Guidelines for Performance Evaluation of Earthquake Resistant Reinforced Concrete Buildings (draft), 2004.
2) Yoon, R., Sanada, Y. and Akahori, T.: Journal of Advanced Concrete Technology, Vol.15, pp.5 44-557,2017.
3) Akahori, T.: Master Thesis, Department of Architectural Engineering, Osaka University, 2016.
4) Akiyama, M., Naito, H. and Suzuki, M.: Journal of JSCE, Vol.58, No.725, pp.113-129,2003.

CFD Study on KCS Maneuvering in Calm Water

Seemontini RoyChoudhury

Hull Form Design Sub-Area, Department of Naval Architecture and Ocean Engineering

Key Words: *CFD, Ship Motions, Neutral Rudder angle, Flow field visualizations, Free Maneuver*

1. Introduction

As assessed in the reports by the Maneuvering Committee of the International Towing Tank Conference[1], modern prediction tools for ship maneuverability mainly include empirical formulae, full-scale trials, model tests (also known as Experimental Fluid Dynamics, EFD), system identification and numerical simulation. The conventional prediction mechanism for ship maneuvering is model testing, which provides direct and reliable assessment of the maneuvering characteristics but is costly and time consuming and most significantly the flow field is seldom measured. Alternatively, Computational fluid dynamics (CFD) provides answers to the pitfalls of model testing by providing flow field visualization at any given point and time of a maneuvering ship. The visualizations are an aid in understanding the mechanism of the ship maneuver. In recent years CFD simulations have progressed from captive to free-running six degrees of freedom (6DOF) conditions. Zigzag maneuvers of KRISO Container Ship (KCS) implementing an actual propeller model using Delayed Detached Turbulence Model has been investigated[2]. The approach provided satisfactory results but the computational cost was very high. Reynolds Averaged Navier Stokes (RANS) maneuvering simulation coupled with various propeller modelling for KVLCC2 was studied[3]. Though computationally not as exhaustive, the drawback with the axisymmetric body force propeller model is its inability to provide propeller side and vertical forces.

In this study, we propose an approach of using RANS coupled with Osaka University (OU) propeller model for KCS maneuvering studies. The advantage of this method is that the hull-propeller-rudder interaction is determined without requiring the detailed modelling of the propeller, thereby reducing computational cost. The model also provides the propeller side and vertical forces which is an added advantage to axisymmetric body force model.

2. Methodology

CFD has been used to predict the self-propulsion and free maneuvering characteristics of the KCS model for Froude number 0.26, with six degrees of freedom (DOF) conditions, in calm water, as recommended by CFD workshop 2015[4]. The length between perpendiculars (L_{PP}) of the model ship is 2.7m for which measurements have also been carried out at IIHR Wave Basin, University of Iowa.

The grid comprising of 11 blocks has been generated using Gridgen. Thereafter SUGGAR library has been used for the overset of grids. CFDShip-IOWA V4.5 (which is an overset, block structured, and incompressible URANS code coupling with motion solver) has been used for numerical prediction. The k-ω SST turbulence model was employed using no wall function. A single phase level-set method has been used to model the free surface and 6DOF ship motions are considered. The computational domain and boundary condition is shown in Fig. 1
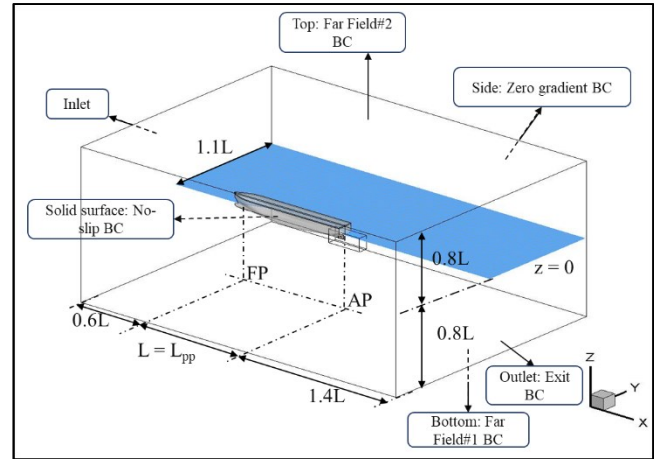

Fig. 1 Computational domain and boundary conditions.

3. Results

3.1 Self propulsion

KCS is a single screw single rudder ship fitted fitted with right handed propeller, thus moves portside when the rudder angle is set to zero. It is therefore necessary to rotate the rudder on the starboard side to maintain straight ahead condition. This angle is known as neutral rudder angle. The self-propulsion in calm water was performed with both rudder and propeller equipped with PID controller. The obtained self-propulsion factors are placed at Table 1.

Table 1 Self Propulsion factors.

Parameter	CFD	EFD	% Deviation
n'	33.61223	37.72000	10.890
δ (deg)	0.77416	0.75000	-3.221
u/U	1.00117	1.00000	-0.117
Thrust (N)	6.39354	6.57000	2.686
Sinkage	0.00207	0.00220	6.062
Trim	-0.13093	-0.11000	-19.024

The local flow field were compared with OU PIV measurement data at a location behind the rudder (x/Lpp =1.025) as shown in Fig. 2. The grid used is able to resolve the two vortices near the hub. The vortex induced vertically lower portion of the propeller along with the vortex induced near starboard upward propeller is also predicted. Thus the same grid was further used in maneuvering simulations.

3.2 Zigzag 20°/20° Maneuvering

The comparison between CFD and EFD results of zigzag maneuvers has been undertaken for $\pm10°/10°, \pm20°/20°$ Results for only 20°/20° have been shown in Fig. 3. Fig. 4 shows the free surface elevation corresponding to point A (maximum yaw), B (zero yaw starboard to port), C (zero yaw port to starboard) and D (minimum yaw) marked on Fig.3. At point B and point D, ship and

propeller wakes are aligned and follows the trajectory. At point A, the rudder is deflected to port side thus the ship wake near the free surface is directed to port. The propeller is still at starboard with propeller wake following the trajectory. Thus the wake is split in two directions.
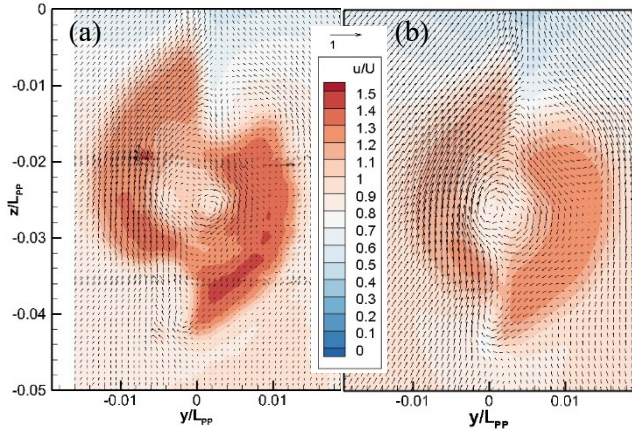

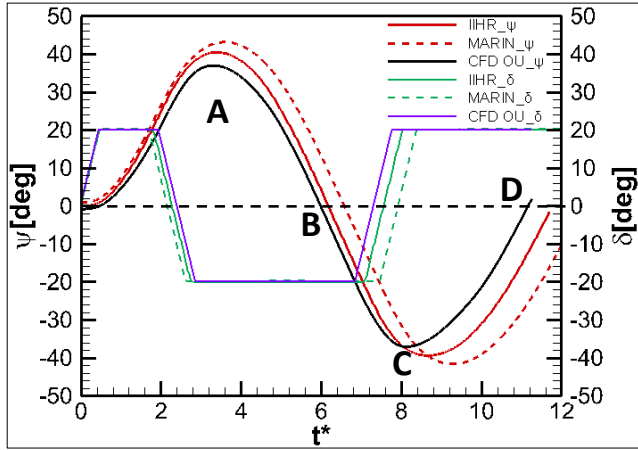Fig. 2 Local flow comparison at x/Lpp =1.025 (a) OU PIV (b) OU CFD.

Fig.3 Starboard side zigzag 20°/20°

Fig. 4 Free surface elevation for zigzag 20/20 at maximum yaw(A), Zero yaw (B and D) and Minimum Yaw (C).

Fig.5 Turning Circle portside maneuver.

3.3 Turning Circle

The comparison between CFD and EFD results of turning circle maneuvers has been undertaken for $\pm 35°$. Results for only -35° have been shown in Fig. 5. The trajectory is under predicted with 35° rudder angle. This could be attributed to the simplified rudder geometry used for this study leading to higher rudder force prediction and higher speed drops at higher angles of attack. To analyzed the stated reason, the turning circle maneuver was performed for 31° and 30° rudder angle. The predicted trajectory with 30° rudder angle matched well with the EFD data thus establishing the need to accurately model the rudder geometry.

4. Conclusions

The predicted self-propulsion factors show good agreement with the EFD data. The propeller revolution is under predicted as the open water chart for IIHR was not used for computations. In addition, the CFD wake field at the analyzed plane shows very good agreement with PIV measurements.

The turning circle maneuver is underpredicted for 35° rudder angle due to overprediction of the rudder force. With lesser rudder angle, the prediction was improved.
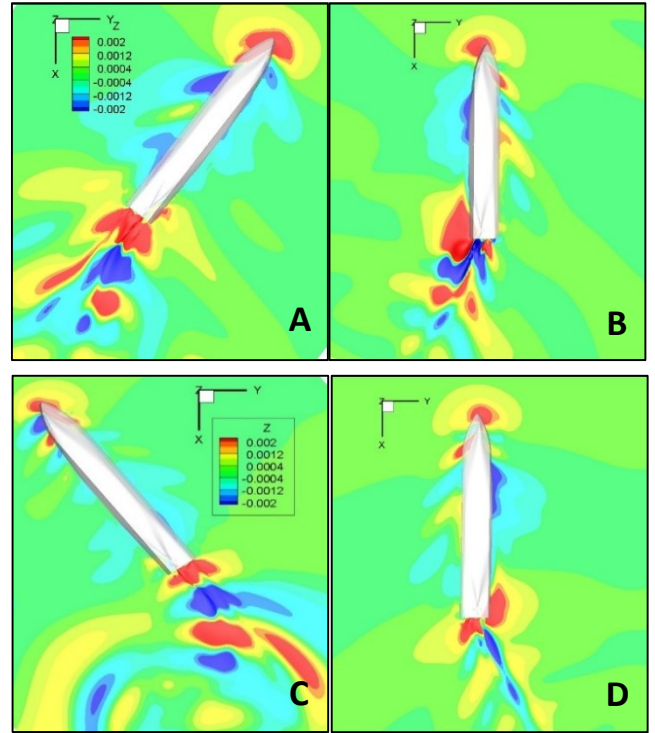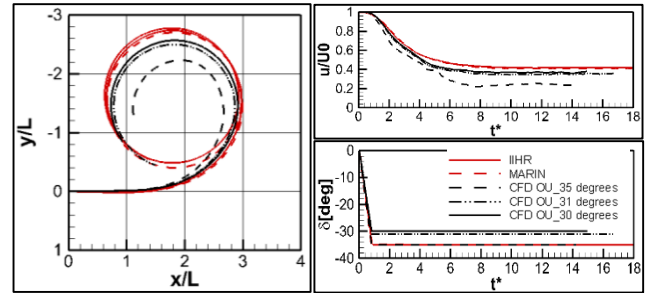
The zigzag maneuver shows good agreement with the EFD data. The maneuvering flow field was analyzed. CFD is undeniably attractive to provide analysis and visualization of the flow.

For future work, the rudder geometry will be improved to incorporate the real geometry. Simulations for course keeping in waves will be performed and analyzed in detail.

References

1) The Manoeuvring Committee.: Final Report and Recommendations to the 25th ITTC, Vol. Ⅰ, Proc. of 25th ITTC, 2008.
2) Mofidi, T. and Carrica, P.M.: J of Computers and Fluids, Vol.96, pp.191-203, 2014
3) Hosseini, H.S, Wu P.C. and Stern F.: CFD simulations of KVLCC2 maneuvering with different propeller modeling, Proc. of Workshop on Verification and Validation of Ship Maneuvering Simulation Methods (Lyngby, Denmark), 2014.
4) http://www.t2015.nmri.go.jp/Instructions_KCS/Case_2.10/Case_2-10.html

Parameter Estimation of a Distributed Hydrological Model in the Ibo River Basin Using the Polynomial Chaos Expansion Method

Putika Ashfar Khoiri

Water Engineering Laboratory, Department of Civil Engineering

Key Words: *Hydrologic prediction, Distributed Hydrological Model, Parameter estimation, Polynomial Chaos Expansion*

1. Introduction

Water discharge prediction is important in order to improve flood management. Modeling actual hydrology systems in river watersheds is difficult because accurate modeling needs to represent land use and other properties of the watersheds. A distributed hydrological model (DHM) is an adequate tool to represent spatial information for each sub-catchment of the watersheds.[1] This prediction is sometimes poor due to various uncertainties in the model and observations. One of their sources is inaccurate parameter estimation, resulting large misfit arises between observed and simulated discharges. In order to reduce the misfit, in this research, polynomial chaos expansion (PCE) is utilized for the parameter estimation. In previously research, PCE techniques have been applied to estimate time-dependent values for two-biological parameters in an ocean model [2] and other engineering applications. However, the PCE application for hydrological model is rarely used. The objectives of this study are to verify the applicability of PCE in DHM by revealing the parameter combinations and its statistical significance to improve simulation results.

2. Parameter estimation method

In this study, an emulator of the polynomial chaos expansion (PCE) method was adopted to estimate model parameters in DHM in order to improve the accuracy of simulated discharge. Parameter (θ) with uniform distribution were adapted to a Legendre-Chaos polynomial. Only two parameters can be optimized in one parameter space.[3] General expression of the Legendre polynomial used in this study is Eq. (1)

$$f(\theta, x_t, u_t) = \sum_{k=0}^{k_{max}} a_k(x_t, u_t)\emptyset_k(\theta) + \in_{trunc}(\theta) \qquad (1)$$

where, $f(\theta, x_t, u_t)$ = distributed hydrological model output, $a_k(x_t, u_t)$ = expansion coefficients of uncertain input θ in the terms of distance and velocity within time, $\emptyset_k(\theta)$ = polynomial of order k in the parameter space defined by θ, k_{max} = the maximum order of polynomial, $\in_{trunc}(\theta)$ = truncation error, for the $k_{max} = \infty$, the approximation is exact and $\in_{trunc}(\theta) = 0$. N_k = normalization factor specific to the kth polynomial and independent of θ. Here, maximum order of Legendre polynomial in Eq. (1) with ($k_{max} = 6$) used for both parameters in each simulation. Then, 49 model runs of two parameters combination are required. The results obtained is the global minimum RMSE from two parameter simulation results.

Due to the orthogonally of the polynomials, conditional expectation and variance are given by Eq. (2), (3)

$$E(f(x, u, \theta)|\theta) = a_0 t \qquad (2)$$

$$var(f(x, u, \theta)|\theta) = \sum_{k=1}^{n} a_k{}^2(x, u)N_k \qquad (3)$$

3. Calculation methods
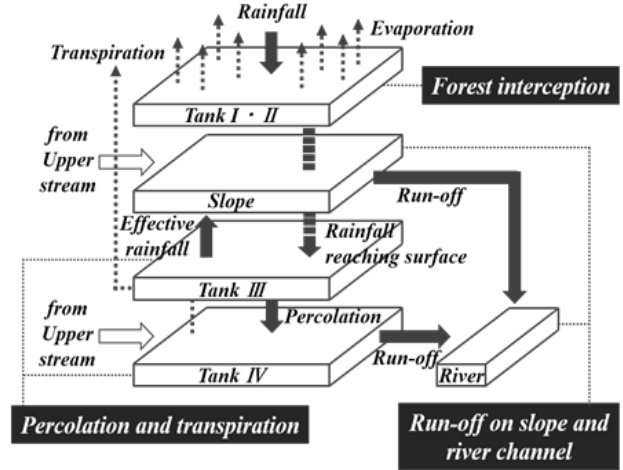
3.1 Distributed Hydrological Model

Fig. 1 The schematically diagram of distributed hydrological model used in this study. [4]

Figure 1 shows the structure of Distributed Hydrological Model used in this study[4] This model consists of 3 sub-model: 1) forest blocking and evapotranspiration sub-model, 2) penetration and transpiration sub-model, and 3) slope and river channel outflow sub-model. In the forest sub-model, the arrival rainfall is considered as a forest layer. Rainfall reached the crown of the forest canopies and moves to the ground surface after filling tank I (the crown part) and tank II. After water in tank II reached its maximum storage, the water outflows over ground surfaces. When the water in the tank II exceeds the limit, the water moves to tank III next. In the penetration and transpiration sub-model, the rain water migrates to soil, and stored into tank III and IV. The storage functions methods in Eq. (4) is used for the calculation.

$$\frac{ds_i}{dt} = r_i - Q_i, \quad S_i = K_i \cdot Q_i^{P_i} \qquad (4)$$

where, S_i : storage of tank i (mm), t : period (h), r_i : effective amount of rainfall (mm/h), Q_i = runoff height (mm/h), K_i : storage constant of tank i, P_i = storage power constant of tank i, i : tank number （III or IV）.

In the slope and river outflow sub-model, the kinematic wave model given in Eq. (5), (6) is used.

$$\frac{\partial h}{\partial t} + \frac{\partial q}{\partial x} = R_e \qquad (5)$$

$$q = \beta \cdot h^m \qquad (6)$$

where, h = water depth (mm), q : unit width discharge (mm²/ sec), x = distance from the top edge of the grid (mm), β, m = model parameters.

3.2 Study area, Data and calculation setting

The study area is the Ibo River basin in Hyogo Prefecture, Japan. The area is divided into 197 grids. The size of the grids is 2 km x 2 km. The discharge observation stations are located at Tatsuno, Yamazaki and Kamigawara. Hourly observed water discharge in 2015 was used.[5] The input data are hourly precipitation data from XRAIN with 250 m x 250 m resolution from January 1st, 2015 to December 31st, 2015. The period of calculations is separated into three parts, which is in the period of large flooding, medium flooding, and the period before large flooding occurs. Sensitivity analysis was conducted before the parameters is put for estimation and the effect of parameter optimization on simulation is evaluated. Parameter estimation was performed in 4 cases with the target parameters which were storage constant of tank III and IV (K_3, K_4), maximum storage in tank I (S_1), layer A-thickness (D), and effective soil layer thickness of 16% and 50% runoff (D_{16}, D_{50}).

4. Results and discussion

All parameters have not been estimated here, while only parameters that have high sensitivity for discharge simulations are determined. The estimated parameters vary in space and time. For example, at Kamigawara station, based on results from the series of sensitivity analyses, parameters D_{16} and K_4 were selected as a target to be estimated (see Table 1). The parameters D_{16} and K_4 are put into PCE calculations and the optimum values of these two parameters were obtained.

The simulated discharge is better reproduced when using the optimum parameter values. During the period of large discharge from June 20th, 2015 to August 15th, 2015, at Yamazaki station, the combination of maximum storage in tank I (S_1) and storage constant in tank III (K_3) give a largest effect on simulated discharge by reduce the RMSE by 29 % from the initial simulation.
The amount of discharge increased during the large discharge period in the case with estimated parameters in Kamigawara station and Tatsuno station, the peak discharge on July 18th, 2015 is higher than initial simulation (see Fig.2).

Table 1. List of optimum parameter value during large discharge period.

Kamigawara

Parameter name	Parameter value	RMSE	
		Initial	PCE
Effective soil layer thickness, of 16% runoff (D_{16}) (mm)	11	18.66	14.2
Storage constant of tank IV (K_4) ($mm^{23/25}h^{2/25}$)	90		

Tatsuno

Effective soil layer thickness, of 50% runoff (D_{50}) (mm)	40	24.08	20.56
Storage constant of tank III (K_3) (hour)	6		

Yamazaki

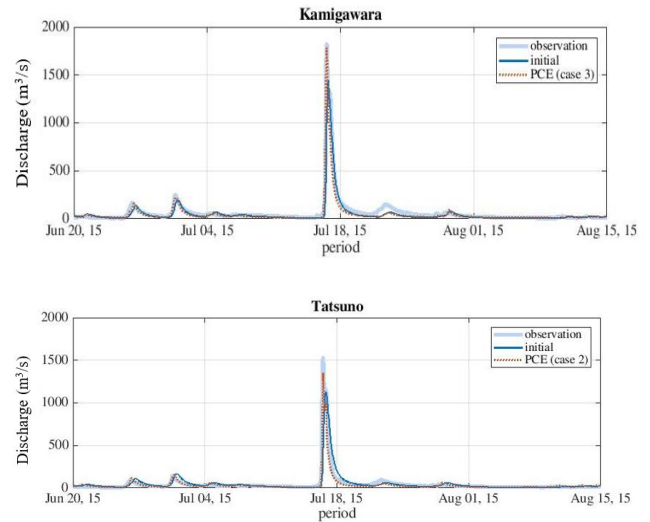|			
Maximum storage in tank I (S_1) (mm)	2.16	21.7249	15.25
Storage constant of tank III (K_3) (hour)	4		

Fig. 2. The results of simulated discharge estimated by PCE

Because the PCE method can estimate the limited number of parameter, further development is required for better optimization of all parameters in DHM. In addition, further evaluation to know the effect of rainfall data distributions should be carried out to obtain more accurate discharge simulation.

5. Conclusions

The parameter estimation method by PCE is capable to reduce the misfit between observed and simulated discharges in the Ibo River basin at 3 observation stations. The storage function of tank III and IV (K_3, K_4) with other parameters is important and substantial to acquire the better simulation. The PCE method can minimize the amount of exhaustive sampling to obtain optimal setting of parameters.

References

1) Fukushima, Y. : A model of river flow forecasting for a small forested mountain catchment , Hydrological Processes , Vol.2, pp.167-185, 1988

2) Mattern, Jann Paul., Fennel, Katja., Dowd, Michael.: Estimating time-dependent parameters for a biological ocean model using an emulator approach. Journal of Marine Systems. 96-97. pp. 32-47, 2012.

3) Xiu, D.B., Karniadakis, G.E.: The Wiener–Askey polynomial chaos for stochastic differential equations. SIAM J. Sci. Comput. 24 (2), pp. 619–644, 2002.

4) Oda, K., Irie, M., Toi, H., Ishizuka, M., Tanaka, K.: Parameter estimation of a distributed hydrological model using an adjoint method, Journal of JSCE B1 (Hydraulic Engineering) (submitted).

5) Ministry of Land, Infrastructure, Transport and Tourism : Hydrological and water quality database, http://www1.river.go.jp, accessed on 2018/3/31.

Motion Analysis of ROV Coupled with Tether

Thant Zin Htun

Marine Mechanical System Engineering Laboratory

Naval Architecture and Ocean Engineering Department, Osaka University

Key Words: *ROV, tethered cable, ANCF, Boundary condition, Numerical simulation*

1. Introduction

Continuous explorations by humans to extend their accessibilities in the deep oceans are demanding a drastic increase in the deployment of underwater vehicles such as AUVs (Autonomous Underwater Vehicles) and ROVs (Remotely Operated Underwater Vehicles) in the deep oceans. Thanks to the real-time telepresence to give the operator a sense of being in the place of the machine, and continuous real-time data transmission, the tether-operated underwater systems have been the favored ones among existing means in deep sea's explorations. ROV can be upgraded by mounting additional equipment to expand the vehicle's capabilities. The tether in low tension state, meanwhile, significantly affects the ROV's motions by creating bending and torsional moments combined with hydrodynamic forces acting on it. The interactions between ROV and tether in real operations complicate the job of ROV's operators. Therefore, an accurate motion simulator is prerequisite for training the ROV's pilots and of predictive assessments.

In this study, a numerical motion analysis of ROV coupled with tether is developed by using 24 dof ANCF (Absolute Nodal Coordinate Formulation)[1] beam elements for kinematics of the tether, which can also account for the torsion and shear. The mathematical modelling of ROV's motion is developed by using hydrodynamic coefficients, which were obtained by the numerical forced oscillation method presented in the previous research[2]. The elastic forces developed in the tether, thrusters' forces, and hydrodynamic forces are treated as the external forces. In the preceding works[3,4], the authors presented initial curl effect of the tether on ROV's motion and defined the boundary condition between the tether and ROV by applying gradient deficient cable beam elements which cannot describe torsion and shear. The anisotropic bending stiffness of the tether was also investigated by conducting cantilever bending test for four different directions.

The focus of this research is to modify the previous research and develop fully-coupled motion analysis between ROV and tether. In this research, the authors presented the effect of torsional moment restored in tether on ROV's yaw motion, and to modify initial conditions of the tether and boundary condition between the tether and ROV. Internal viscous damping was implemented into the motion equation of cable and its effect on cable motion is also discussed. The internal damping forces and torsional rigidity of the tether are evaluated, developing a torsional pendulum simulation and the results are validated by conducting the torsional pendulum experiment of the cable. The torsional effect of the tether on ROV's yaw angle is also discussed by performing turning test of ROV in simulation.

2. CU-ROV and Tether

2.1 Overview of CU-ROV

CU-ROV, which was developed by JAMSTEC is used as the sample ROV in this research. It is equipped on the Deep Sea Scientific Drilling Vessel "CHIKYU" and used for observation of the drilling points and drilling holes on reinstallation of the drilling pipes. Two LED lights and a wide-angled camera are mounted at the front of the ROV to provide visuals for the pilot,

and it is propelled by a total of five propellers, two of which are installed on the upper face while the other threes, at the stern. The principle dimensions and characteristics of CU-ROV are shown in Table 1 and Fig. 1.

Table 1　Characteristics of CU-ROV

Weight in air	34.65 kg
Length×Breadth×Height	0.6 m×0.365m×0.325m
Speed	0～2.0 knot
Operational depth	7000 m

Table 2　Characteristics of Tethered Cable

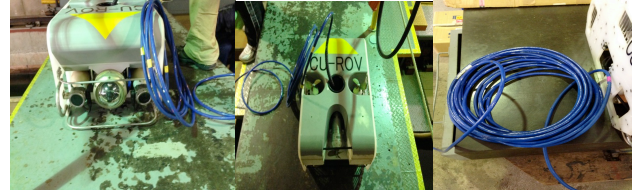| Weight per unit length	0.1342 kg/m
Diameter	0.01 m
Cross section area	7.854×10^{-5} m^2
Geometric Moment of inertia	4.909×10^{-10} m^4

Fig.1 Overview of CU-ROV (developed by JAMSTEC)

2.2 Modelling Motion Equation of ROV

The dynamics of the ROV is described by the motion in the body-fixed coordinate system which is defined at the ROV's geometric center.

$$\mathbf{M}\dot{\boldsymbol{v}} = \boldsymbol{\tau} \tag{1}$$

$$\dot{\boldsymbol{v}} = \{\dot{u}, \dot{v}, \dot{w}, \dot{p}, \dot{q}, \dot{r}\}^T, \boldsymbol{\tau} = \left[F_x, F_y, F_z, M_x, M_y, M_z\right]^T \tag{2}$$

where $\mathbf{M}$ accounts for the total mass matrix of ROV, $\dot{\boldsymbol{v}}$ is the acceleration vector and $\boldsymbol{\tau}$ represents the generalized external force vector applied on ROV.

2.3 Modelling Motion Equation of the Tether

A non-incremental absolute nodal coordinate formulation (ANCF) for three-dimensional beam elements is used to analyze the kinematics of the tethered cable. In this formulation, the position of each node is described by absolute nodal coordinates and gradients of the positions with respect to material coordinates instead of infinitesimal angles. A distinguishing feature in ANCF is the use of slope vectors to describe the orientation of the cross-section of the beam, thus, continuity of slope is achieved. This method leads to a constant mass matrix.

$$\boldsymbol{e} = \left[r_i^T \; r_{i,x}^T \; r_{i,y}^T \; r_{i,z}^T \; r_{i+1}^T \; r_{i+1,x}^T \; r_{i+1,y}^T \; r_{i+1,z}^T\right]^T \tag{3}$$

$$\boldsymbol{r} = S(x, y, z)\boldsymbol{e} \qquad (4)$$

$$S = [S_1\boldsymbol{I} \quad S_2\boldsymbol{I} \quad S_3\boldsymbol{I} \quad S_4\boldsymbol{I} \quad S_5\boldsymbol{I} \quad S_6\boldsymbol{I} \quad S_7\boldsymbol{I} \quad S_8\boldsymbol{I}] \qquad (5)$$

where S is the element shape function for 24 DOFs beam, and each node is defined by the position vector r and the three gradient vectors $r_{,x}, r_{,y}, r_{,z}$.

$$(M + M_a)\ddot{\boldsymbol{e}} + C_{ID}\dot{\boldsymbol{e}} + K_1\boldsymbol{e} + K_b(\dot{\boldsymbol{e}} \text{-} \boldsymbol{e_0}) + K_t(\boldsymbol{e} \text{-} \boldsymbol{e_0}) = \boldsymbol{Q}_f \qquad (6)$$

where M and M_a represents the element mass matrix and added mass matrix respectively. $\boldsymbol{e_0}$ represents the initial coordinate vector of the cable, and ($\dot{\ }$) is the differentiation of global coordinate vector w.r.t time. C_{ID} is the internal viscous damping factor and K_1, K_b, K_t represent the stiffness matrices corresponding to the axial deformation, bending and torsion respectively. $\boldsymbol{Q}_f$ represents the generalized external force vector.

2.4 Boundary Condition between the Tether and ROV

The boundary condition is defined such that the cable's center line at the sling point, which is exactly same as the tangential vector of the cross-section of the Euler-Bernoulli's beam, coincides with the negative normal vector of the ROV's upper surface. The coupling terms are, thereby, established between ROV and the tether at the attached node.

$$\mathbf{n}' = \mathbf{E}\,\mathbf{n} = \begin{bmatrix} cos\theta cos\psi & cos\theta sin\psi & -sin\theta \\ sin\phi sin\theta cos\psi - cos\phi sin\psi & sin\phi sin\theta sin\psi + cos\phi cos\psi & sin\phi cos\theta \\ cos\phi sin\theta cos\psi + sin\phi sin\psi & cos\phi sin\theta sin\psi - sin\phi cos\psi & cos\phi cos\theta \end{bmatrix}\begin{bmatrix} 0 \\ 0 \\ -1 \end{bmatrix}$$

$$\{\boldsymbol{r}_{i\_sling,z}\} = \begin{bmatrix} cos\phi & sin\theta & 0 \\ -sin\theta & cos\phi & 0 \\ 0 & 0 & 1 \end{bmatrix} \cdot \{-\mathbf{n}'\} \cdot |\boldsymbol{r}_{i\_sling,z}| \qquad (7)$$

where $\mathbf{E}\ (\varphi, \theta, \psi)$ is the Euler's rotation matrix, $\mathbf{n}'$ represents the negative normal vector of the ROV's upper face, and $\boldsymbol{r}_{i\_sling,z}$ is the gradient vector along the center line of the cable at the sling point.

Fig. 2 Boundary Condition between ROV and Tether

3. Conclusions and Future Endeavors

3.1 Conclusions

In this research, the stiffness matrices and constant mass matrix that can also account for rotary inertia in three dimensional 24dof beam were explicitly presented. The cable is considered as a very slender beam, i.e., the shear of the tether was neglected in this work. The author also presented the coupling interaction between the tethered cable and ROV's six degrees of freedom motion. The boundary condition between the tether and ROV at the sling point was clearly expounded. The implementation of torsion effect was presented by carrying out the simulation of the turning maneuver in both clockwise and counter-clockwise directions.
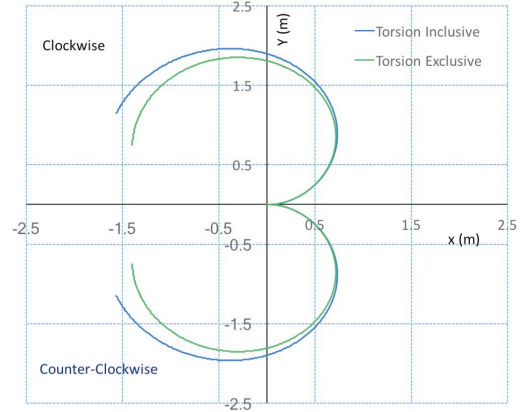

Fig. 3 Trajectories of ROV's Turnings (Showing the Effect of Torsional Moment Restored in Tether on ROV's Turning Motion Propelled by Port /Starboard Side Thruster with 6 rev/s for Each Direction in Simulation)

3.2 Future Endeavors

In the present work, Berzeri's T1 model (Berzeri and Shabana)[5] was used to develop the bending forces of the finite elements for better simulation execution. In this model, the constant curvature assumption is used when the longitudinal deformation is not quite large. However, it has been observed that the program converges slowly when increasing the number of elements for thin beam models compared to other beam models. That convergence problem is due to constant bending strains over the length of the element. Meanwhile, the inclusion of torsion effect to the tether shows considerable effect on ROV's yaw motion. In the current work, the assumed shape function is obtained by applying linear interpolation in x and y directions and cubic interpolation in z direction, where the z direction is initially along the central axis of the beam. To improve the accuracy of bending and torsional effects, higher order elements will be used by introducing additional shape functions[6]. The depth varying ocean current velocity, and the movement of mother ship and cage will also be taken into account in the cable dynamics.

References

1) Shabana, A. A., Hussien, H. A., and Escalona, J. L.:Application of the Absolute Nodal Coordinate Formulation to Large Rotation and Large Deformation Problems, ASME J. Mech. Des., Vol.120, pp.188-195, 1998.
2) Suzuki, H., Yoshida, H., Inoue, T.:Evaluation of Methods to Estimate Hydrodynamic Force Coefficients of Underwater Vehicle Based on CFD, Proc. of the 9th IFAC Conference 2013(*CAMS*2013).
3) Suzuki, H., Tomobe, H., Kuwano, A., Takasu, K., Inoue, T., Ishiwata, J.:Numerical Analysis of the Motion of ROV Applying ANC Method to the Motion of Tethered Cable, Proc. of the ISOPE Conference, pp.447-453, 2017.
4) Suzuki, H., Tomobe, H., Kuwano, A., Takasu, K., Thant Zin Htun :Numerical Motion Analysis of ROV applying ANCF to Tether Cable Considering its Mechanical Property, Proc. of the ISOPE Conference, pp.365-372, 2018.
5) Berzeri, M., Shabana, A. A.:Development of Simple Models for the Elastic Forces in the Absolute Nodal Coordinate Formulation, Journal of Sound and Vibration, Vol.235, No.4, pp.539-565, 2000.
6) J. Gerstmayr, A.A. Shabana :Analysis of Thin Beams and Cables Using the Absolute Nodal Coordinate Formulation, Nonlinear Dynamics, Vol.45, pp.109, 2006.

Minimum Propulsion Power Prediction of a Ship under Adverse Weather Conditions with Dynamics of Diesel Engine and Turbocharger Taken into Account

Myo Zin Aung

Ship Design Subarea, Department of Naval Architecture and Ocean Engineering

Key Words: *Minimum Propulsion Power Requirements, Mean Value Engine Model, Turbocharger, Bulk carrier*

1. Introduction

To reduce the amount of greenhouse gas emissions from international shipping and to encourage increasing the efficiency of the new ships at the design stage, IMO adopted the EEDI regulations in Annex VI of MARPOL convention. EEDI means Energy Efficiency Design Index and it is measured in CO2 g/ton-nmile. Therefore, higher EEDI value means more CO2 emission from a ship. EEDI regulation limits the amount of CO2 emission from ships and this regulation will be gradually tighten phase by phase every 5 years starting from 2015. Since EEDI is proportional to the ship's propulsion power and the power is also roughly proportional to the cube of ship's speed, ship design speed reduction is the easiest response to the EEDI requirement.

Although the main purpose of EEDI is to encourage for the development of more efficient ships, it becomes a limit for maximum power when expensive new technologies and low emission fuels are not used. In the near future, the ship owners and designers may reduce the installed propulsion power just to comply with EEDI regulations. Simple reduction of engine power could result in operational danger under adverse weather conditions. Therefore, IMO also adopted a guideline for minimum propulsion power.

To improve this guideline, manoeuvring simulations in adverse weather conditions are essential for the assessment of navigational safety due to propulsion power deficiency. EU project SHOPERA and JASNAOE projects (Ohiwa and Umeda, 2016) contributed to discussion on the guideline at the IMO. Better numerical prediction models with precise modelling of wave drift forces, wind forces and manoeuvring forces were also developed. However, their engine models were based on the diagram of engine speed and power without explicit consideration of engine-turbocharger and so on. Since the minimum propulsion requirements are directly related to dynamics of diesel engine and turbocharger, more precise modelling of diesel engine and turbocharger is desirable. Thus, in this work, the author proposes a new prediction model with a more precise engine-turbocharger model in the time domain and executes manoeuvring simulations of a Handymax bulk carrier under adverse weather conditions to access its safe navigational limit.

2. Manoeuvring Model

2.1 Equations of Motion

For the maneuvering simulations, 4 DOF equations of motion are represented as follow using the MMG model and the relevant standard symbols (Ohiwa and Umeda, 2016):

$$(m + m_x)\dot{u} - (m + m_y)vr$$
$$= X_H + X_P + X_R + X_A + X_W \qquad (1)$$

$$(m + m_y)\dot{v} + (m + m_x)ur - m_y l_y \dot{p}$$
$$= Y_H + Y_R + Y_A + Y_W \qquad (2)$$

$$(I_x + J_x)\dot{p} - m_y l_y \dot{v} - m_x l_x ur + 2d_1\dot{\phi} + d_2\dot{\phi}|\dot{\phi}|$$
$$+ mg\overline{GM}\phi = K_H + K_R + K_A \qquad (3)$$

$$(I_z + J_z)\dot{r} = N_H + N_R + N_A + N_W \qquad (4)$$

2.2 Environmental Forces and Moments

The wind forces and moments are estimated with the Fujiwara's empirical formula (Fujiwara 1998). The added wave resistance for different ship speeds are estimated by Maruo's theory (Maruo 1963). The wave-induced steady sway force, and yaw moment are calculated by a linear 3D panel method using the Green function for zero forward speed (Yasukawa et al., 2018). These wave-induced steady forces and moments in irregular waves are calculated with the JONSWAP wave spectrum by assuming they are proportional to the square of wave height.

3. Mean Value Engine Model for Propulsion System

The main contribution of this thesis is to include the engine-turbocharger and governor model in the manoeuvring simulation. For the engine-turbocharger modelling, cycle mean value approach is used as shown in Fig. 1 whereas the governor is designed using PI controller with the integral wind-up action.

Fig. 1 Engine Components and Operating Parameters.

The engine-turbocharger model was split into different subsystems as shown in Fig. 1; the compressor, turbine, intake manifold, exhaust manifold and engine cylinders. Each part was modelled using physical principles, and information was exchanged between them with the means of flow of mass and energy.

3.1 Dynamics of Engine Assembly

The dynamics at the crankshaft, turbocharger, intake (scavenging) manifold, exhaust manifold are represented as follow. Using the Newton's law, crankshaft and turbocharger dynamics are modelled as follows (Karlsen 2012, Xiro 2002):

$$\dot{\omega}_E = \frac{Q_E - Q_P - Q_f(\omega_E)}{J_{total}} \tag{5}$$

$$\dot{\omega}_{TC} = \frac{Q_T - Q_C}{J_{TC}} \tag{6}$$

Using the first law of thermodynamics, adiabatic formulation of intake and exhaust manifold dynamics are as follows (Karlsen 2012, Guzzella, Onder 2010):

$$\dot{p}_{im} = \frac{\kappa_a R_a}{V_{im}}(\dot{m}_c T_i - \dot{m}_a T_{im}) \tag{7}$$

$$\dot{T}_{im} = \frac{R_a T_{im}}{p_{im}V_{im}}\left(\kappa_a \dot{m}_c T_i - \kappa_a \dot{m}_a T_{im} - T_{im}(\dot{m}_c - \dot{m}_a)\right) \tag{8}$$

$$\dot{p}_{em} = \frac{\kappa_e R_e}{V_{em}}(\dot{m}_e T_e - \dot{m}_t T_{em}) \tag{9}$$

$$\dot{T}_{em} = \frac{R_e T_{em}}{p_{em}V_{em}}\left(\kappa_e \dot{m}_e T_e - \kappa_e \dot{m}_t T_{em} - T_{em}(\dot{m}_e - \dot{m}_t)\right) \tag{10}$$

3.2 Validation with Manufacturer's Data

The mean value engine model is validated with the steady-state performance data provided by the engine manufacturer (MAN Diesel & Turbo 2016) using the 1 DOF manoeuvring model of Handymax bulk carrier. The engine specified MCR point (design operating point) is 7930 kW at 137 rpm, which corresponds to the heavily running condition. The validation results show the good agreement with the manufacturer's data.
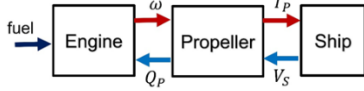
Fig. 2 Interaction of Engine Validation Model Subsystems
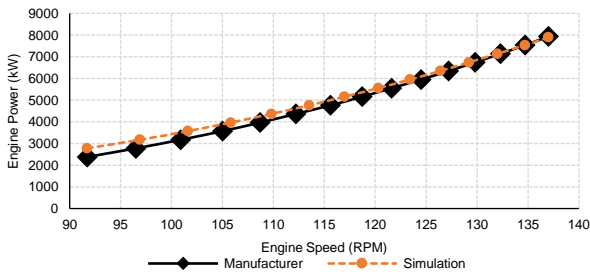
Fig. 3 Heavily Running Engine Design Curve (Propeller Curve)

4. Manoeuvring Simulation in Adverse Weather

The ship is initially assumed to be in following sea condition and it tries to turn to head sea condition using PID autopilot. In this scenario, the ship is able to make turning to the head sea up to Beaufort Scale (BF) No. 10 condition. The final steady-state ship speeds in the head sea are 8.5 knots, 3.0 knots and 0.7 knots for BF No. 8, BF No. 9 and BF No. 10, respectively. Therefore, we may assume that the ship with this particular installed power is safe up to the BF No. 10 weather condition for keeping head sea conditions. The ship trajectories and time series data are shown in Fig.4 and Fig.5, respectively.
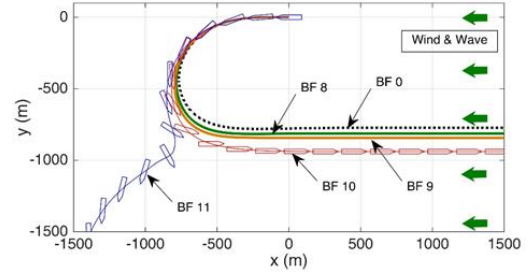
Fig. 4 Trajectories of Ship.
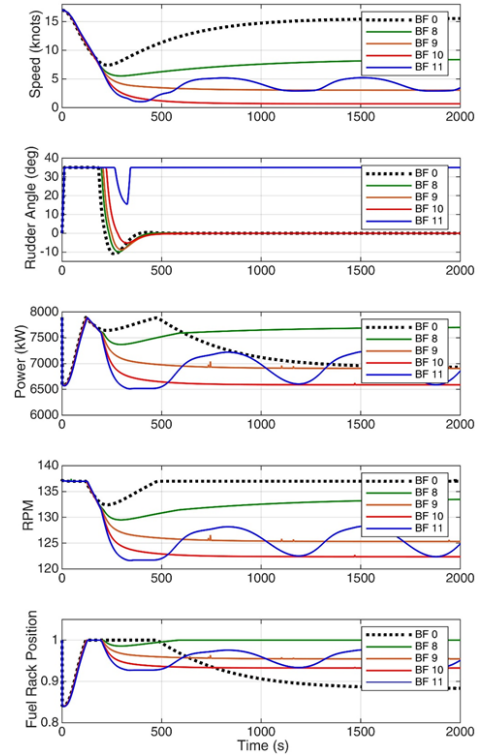
Fig. 5 Time Series Data.

5. Conclusions

A new simulation model for the prediction of minimum propulsion power is proposed using the mean value engine modelling approach for the propulsion system. The proposed engine model is validated with the steady-state performance data provided by the engine's manufacturer. Manoeuvring simulations are executed for a Handymax bulk carrier to observe the dynamics of propulsion engine and to access the safe navigational limit under different weather conditions. The proposed simulation model can scope realistic responses of engine power and rpm which are important when considering the power limit lines defined by these variables. Moreover, the new simulation model is applicable for wider type of manoeuvring scenario since the engine or propeller rpm can be controlled using the governor.

References

1) Ohiwa, S., Umeda N., "Probabilistic aspect on minimum propulsion power requirement issue under adverse weather conditions," Proc. of DfS 2016, Hamburg, pp. 127-131, 2016.

2) Karlsen, T. A. "On modelling of a ship propulsion system for control purpose," Master Thesis, NTNU, Norway, 2012.

3) MAN Diesel & Turbo, Copenhagen, Denmark, "MAN B&W S40ME-B9.5-TII Project Guide," July, 2016.

Structural Analysis of a Floating Vertical Axis Wind Turbine

Ahmad Adilah

4th Laboratory, Department of Naval Architecture and Ocean Engineering

Key Words: *Floating vertical axis wind turbine, Gyroscopic effect, Vertical bending moment*

1. Introduction

In recent days floating Vertical Axis Wind Turbine (VAWT) are attracting researchers' attention. This is because it is more suitable for floating offshore wind turbine than the horizontal ones. It has a low center of gravity, simplicity of the installation and insensitivity to yaw and pitch[1].

There are a few researches that analyze the motion of floating VAWT. Meanwhile, almost no researchers pay attention to the structural analysis of floating VAWT. This analysis becomes more important considering the rapid development of floating vertical axis wind turbine with larger structure in the future.

2. Research methodology

2.1 Two-step method

A practical so-called two-step method is used in which a rigid body model is used to obtain the load distribution, and the distribution of the load is given to a structural model adopted in the second step for stress/deformation analysis.
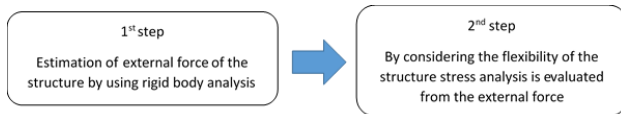
Fig. 1 Block diagram of two-step method

A rigid body numerical simulation procedure for the floating VAWT is developed and compared against the data from experiment result[2]. The simulation can account for the hydrodynamic loads, aerodynamic loads, rigid body motions, gyroscopic effects, Magnus effect, mooring loads, hydrostatic and gravity loads. While evaluate the hydrodynamic load, SPAR structure is divided into short cylinders for numerical evaluation.

Magnus effect is considered when the SPAR rotates in marine current and/or wave. The direction of the Magnus force is perpendicular to the flow and the rotational axis. The magnitude of the force per unit length is,

$$F_{magnus} = \rho_w u_r \Gamma \quad (1)$$

where u_r is the relative flow speed component perpendicular to the cylinder axis. Γ is the circulation around the cylinder, $\Gamma = (\pi d^2/4) \cdot 2\omega_{rot}$. Here, ω_{rot} is the rotational speed of cylinder and d is the diameter of cylinder.

Further, the structural analysis is performed by using the load distribution that obtained from the rigid body analysis. The external force and inertial force of the structure should be balanced while perform the structural analysis. Flexibility of the structure should be considered in this analysis. The load distribution is integrated to obtain shear force, vertical bending moment and finally bending stress distribution of the structure.

2.2 Equations of motion

The equations of translational and rotational motion of the structure are given as follows.

$$F_{morison} + F_a + F_b + F_g + F_{magnus} + F_{mooring} = m\frac{dv}{dt} \quad (2)$$

$$\frac{d}{dt}(I\omega) + \omega \times (I\omega) = \sum M_i \quad (3)$$

where, m is the total mass of the structure, v is the relative velocity vector of the structure, I is the inertial moment matrix and ω is the angular velocity vector of the structure in body fixed coordinate system. F_a is the aerodynamic force that acting on the structure, F_b and F_g is the buoyancy and gravity force of the structure. The rotational moment caused by the total forces are written as M_i. Quaternion is used to rotationally transforming the coordinate system.

2.3 Model of analysis

In this research, a spar structure is used as a floating structure of the turbine to accommodate 1 MW vertical axis wind turbine. The SPAR structure consisting of various diameter. Table 1 shows the structural configuration of spar.

Table 1 Structural configuration of spar

Draft	48.3 m
Upper diameter	3.3 m
Bottom diameter	5.0 m
Shell thickness	24.2 mm

For evaluating the structural behavior, the spar structure is divided into beam elements along the axis. Figure 2b shows the subdivision with beam elements for the spar structure.
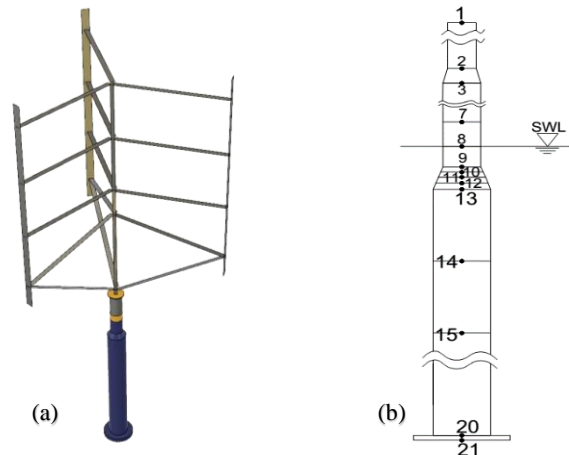

Fig. 2 (a) Floating axis wind turbine and (b) beam element subdivision of the spar structure

3. Result and Discussion

3.1 Rigid body motion

The rigid body motion is simulated in regular wave condition with wave height H is 0.2 m and wave period T varying between 5 s to 12 s.
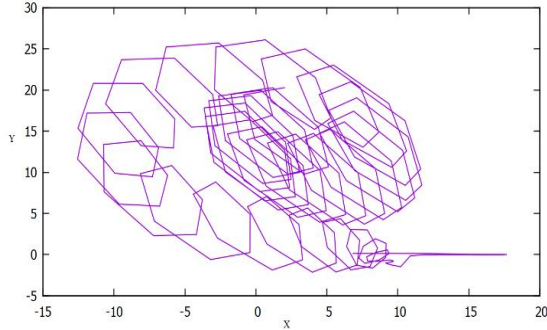

Fig. 3 Trajectory in xy-plane of spar axis in the regular wave. $T = 12$ s

Figure 3 shows the trajectory in xy-plane of the spar axis. The simulation results show that Magnus effect and gyroscopic effects occur in the motion of the structure. The Magnus effect cause the turbine experience the drift motion and the gyroscopic effects contributes to the stabilization of the turbine.

3.1 Structural analysis

Structural analysis is performed under the static (aerodynamic) and dynamic (wave) load condition. Based on the load distribution, we can know the shear force and vertical bending moment distribution along the spar axis. Figures 4 and 5 show the distribution of shear force and vertical bending moment for regular wave with period $T = 12$ s.
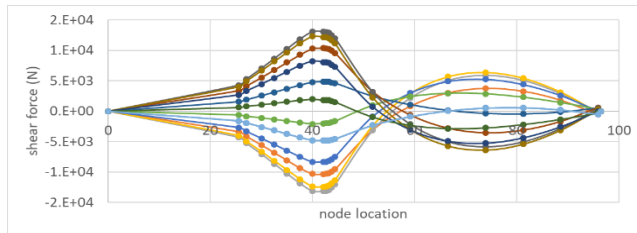
Fig. 4 Shear force distribution along the spar axis. $T = 12$ s
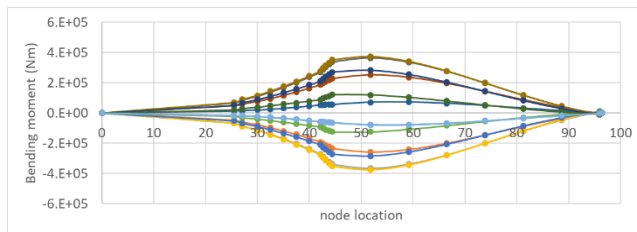
Fig. 5 Vertical bending moment distribution along the spar axis. $T = 12$ s

The zero point in x-axis represent the top of the structures and the bottom position of the structure is 96.5 m. After vertical bending moment is known, the bending stress can be obtained by dividing the vertical bending moment with sectional modulus of the spar.
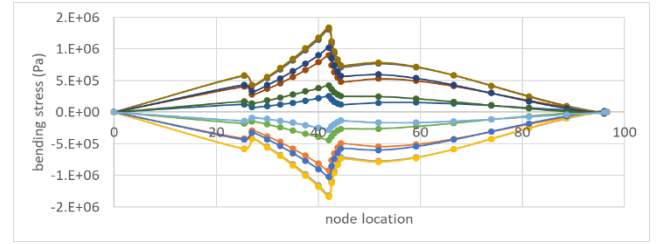
Fig. 5 Bending stress distribution along the spar axis. $T = 12$ s

From the result we can know that the maximum bending stress occurs in element near still-water level, this because of the small cross-section area in the transition part compared to other parts, and large vertical bending moment there.
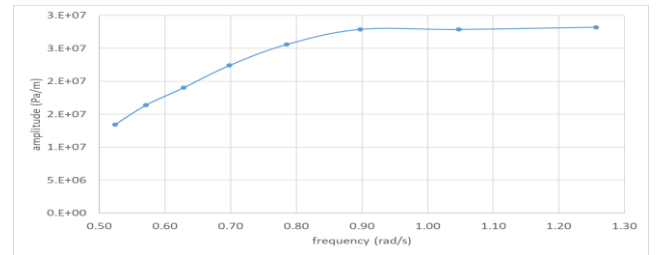
Fig. 6 RAO stress at beam element transition part

By plotting the response amplitude operator (RAO) stress at the element near still-water level for all wave frequency range we can know that the maximum bending stress is about 28.2 MPa per unit wave amplitude. For comparison, the pitch acceleration RAO is presented in Fig. 7. The two curves in Figs. 6 and 7 resemble each other because the inertial load is causing the structural response, which results in the larger stress in higher frequency.
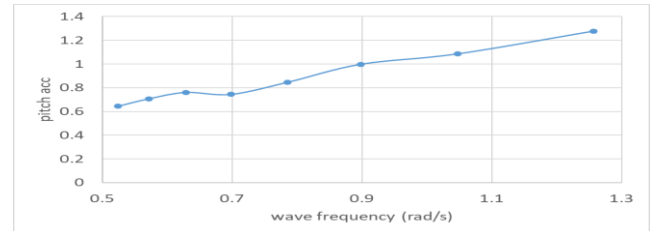

Fig. 7 RAO of angular acceleration of spar structure

For static aerodynamic load case, the maximum bending stress in the transition part is measured to be 123 MPa. It is almost exceeding the yield stress which is 175 MPa, therefore some design modification is necessary.

4. Conclusions

From rigid body simulation, it is found that the turbine experiences the Magnus effect and gyroscopic effect. However gyroscopic effect on turbine enhances the stability of the structure. The maximum bending stress are found about 28.2 MPa for dynamic load case and 123 MPa for static load case.

References

1) H. J. Sutherland et al.: A Retrospective of VAWT Technology, SAND2012-0304, 2015.
2) H. Akimoto.: Floating vertical axis wind turbine simulator SimFAWT (not published)

Numerical Calculation of Ship Hydroelasticity Using Enhanced Unified Theory

ZHOU Dali

Ocean-Space Development Laboratory, Dept. of Naval Architecture & Ocean Engineering

Key Words: Ship *hydroelasticity, Enhanced unified theory, 3D effect, Mode function, Green function method*

1. Introduction

As the main means of transportation, the ship is still keeping popularity in the trading industry over centuries. Since the need for cargo transportation capability is gradually increasing, the dimension of ships becomes larger subsequently. Thus, ships tend to be flexible with increasing the ship length. The deformation of a body, the effect of structure stiffness, and the fluid structure interaction are of much importance in the seakeeping analysis.

Various analysis methods for the global hydroelastic behavior have been developed by many researchers. To name a few among them, we may write as follows. Bishop and Price[1] presented a fundamental concept of the hydroelastic problem using the strip theory. Jensen and Dogliani calculated nonlinear springing load using a nonlinear strip theory. Malenica *et al.* proposed a method combining the frequency-domain 3D boundary integral equation method (BIEM) with the finite element method (FEM) for a non-uniform beam, results of which were compared successfully with experimental data.

Considering these developments so far and a practical requirement that the global hydroelastic response must be computed with reasonable accuracy and less computation time, we need to establish a practical computer code for ship hydroelasticity problems. In this paper, Enhanced Unified Theory (EUT)[2] is applied to the hydrodynamic analysis. For the structural analysis, it is common to define a set of natural mode shapes, which correspond to actual elastic deflections of a body in a specified physical context. The structural deflection is represented by a superposition of these natural mode shapes. Compared to the analysis for a rigid body, an important difference in the hydroelastic analysis exists in the body boundary condition which represents the normal velocity on the body surface induced by the structural deflection. Computed results for hydrodynamic forces and wave-induced motions are validated for the zero-speed case through comparison with more exact results by the 3D Green function method, and then the results for the forward-speed case are presented and discussed.

2. Structural Analysis

2.1 Structural Problem

In the structural analysis, it is common to define a set of orthogonal mode functions[3], which correspond to the actual elastic deflections of a body in a specified physical context. Generally this is difficult when the mode shapes are affected by the hydrodynamic pressure field and cannot be specified in advance. This difficulty can be avoided if the structural deflection is represented instead by a superposition of simpler mathematical mode shapes which are sufficiently general and complete to represent the physical motion.

2.2 Mode function

In the modal superposition method, the total displacement of a ship $H(x,t)$ is expressed by superposition of dry natural mode functions as follows:

$$H(x,t) = \sum_{j=1}^{N} \xi_j(t) h^j(x) \tag{1}$$

where $x = (x, y, z)$ is the position vector, index j denotes the mode number, and $\xi_j(t)$ is the time dependent amplitude of the j-th mode of motion. The mode number $j=1\sim6$ and $j=7\sim N$ correspond to the rigid- and elastic-body motions, respectively, and N is the total number of modes to be considered.

As an example, in the case of vertical bending the components of normalized mode-function vector $h^j(x)$ can be written as

$$h_1^j = 0, \quad h_2^j = 0, \quad h_3^j = w_j \tag{2}$$

where h_1^j has a nonzero component, but due to order estimation with slender ship assumption, it can be regarded as negligibly small. On the other hand, $w_j(x)$ is the vertical displacement in the j-th mode of motion. If the free-free beam modes of a uniform beam are adopted for $w_j(x)$, they are given analytically and their shapes can be given as shown in Fig. 1.
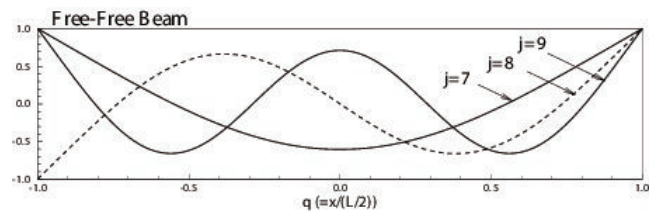

Fig. 1 Vertical displacement in the *j*-th mode of motion

3. Hydrodynamic Analysis

3.1 Computation method

Let us consider a ship advancing with constant speed U and undergoing small-amplitude harmonic motions with angularr frequency ω in deep water. A steady reference frame is chosen with the x-axis pointing to the direction of forward motion and the z-axis pointing downward. The plane progressive wave is incident upon the ship with incidence angle χ, in which $\chi = 180$ deg is defined as head wave.

Assuming the flow inviscid with irrotational motion, the velocity potential is expressed as

$$\Phi = -Ux + \text{Re}[\phi(x,y,z)e^{i\omega t}] \tag{3}$$

$$\phi = \frac{ga}{i\omega_0}\{\phi_0(x,y,z) + \phi_7(x,y,z)\} + i\omega\sum_{j=1}^{6} X_j\phi_j(x,y,z) \tag{4}$$

$$\phi_0 = \exp[-k_0 z - ik_0(x\cos\chi + y\sin\chi)]$$

$$\omega = \omega_0 - k_0 U\cos\chi, \qquad k_0 = \omega_0^2 / g$$

Here ϕ_0 denotes the incident-wave potential, ϕ_7 the scattered potential, and ϕ_j the radiation potential of the j-the mode with complex amplitude X_j. Also a, ω_0, k_0 denote the amplitude, circular frequency, wave number of the incident wave; g the acceleration due to gravity. Besides, the disturbance due to the steady forward motion is neglected as higher order.

3.2 Hydrodynamics force

Integrating the pressure over the mean wetted surface of a ship, and using Tuck's theorem, the hydrodynamic force in the radiation problem[2] acting in the i-th direction can be expressed as

$$F_i = -(i\omega)^2 \sum [A_{ij} + B_{ij}/i\omega]X_j \qquad (5)$$

$$
A_{ij} + B_{ij}/i\omega = -\rho \int_L dx \int_{SH} (\tilde{N}_i - \frac{U}{i\omega}\tilde{M}_i)\{\varphi_j + \frac{U}{i\omega}\widehat{\varphi}_j\}ds
$$
$$
- \rho \int_L dx C_j(x) \int_{SH} (\tilde{N}_i - \frac{U}{i\omega}\tilde{M}_i)\{\varphi_3 - \varphi_3^*\}ds \qquad (6)
$$

where A_{ij} and B_{ij} are the added-mass and damping coefficients in the i-th direction due to the j-th mode of motion, and SH denotes the sectional contour below the free surface at station x. The first line on the right-hand side of Eq. (6) is essentially the same as that in the strip theory and the second line represents the 3D-effect which can be computed in terms of homogeneous component in EUT.

In the diffraction problem[2], the hydrodynamic pressure is given from the sum of the incident-wave and scattered potentials. The symmetric part of the diffraction force can be expressed as

$$
E_j = -\iint_{SH} P_d \tilde{N}_j dS
$$
$$
= \rho g a \int_L dx C_7^s(x) e^{i\ell x} \int_{SH} \tilde{N}_j\{\psi_7^s + e^{-k_0 z}\cos(k_0 y\sin\chi)\}e^{i\ell x}ds \qquad (7)
$$

4. Numerical calculation

Numerical computations are performed for a 2-meter modified Wigley model. The principal dimensions are shown in Table 1.

Table 1 Principal dimensions of modified Wigley model.

Length L	2.000 m
Breadth B	0.300 m
Draft d	0.125 m
Displacement volume ∇	0.04205 m³
Height of the center of gravity OG	0.0404 m
Gyrational radius in pitch κ_{yy}	0.456 m

4.1 Result

The numerical computations were launched for the zero speed case for validation and then for the forward speed case. Computed results by EUT for the radiation force, wave exciting and ship motions are compared with the frequency-domain 3D Green function method for the zero-speed case, the time-domain Green function method, and the Rankine panel method for the forward speed case.

As an example, computed results of the wave exciting force at zero speed for elastic motion (mode number equal to 7, 8 and 9) are shown in Fig. 2, from which we can see god agreement with different methods. In Fig. 3, the results of the amplitude of wave-induced ship motions for both rigid and elastic bodies are presented. Good agreement also could be found except for the elastic mode $j = 8$, for which the result by the frequency-domain 3D Green function method must be something wrong, but the reason of the problem could not be detected up to now.
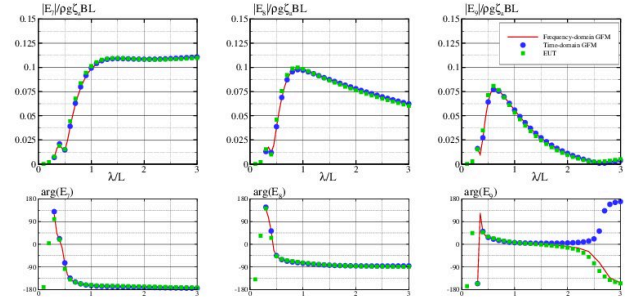

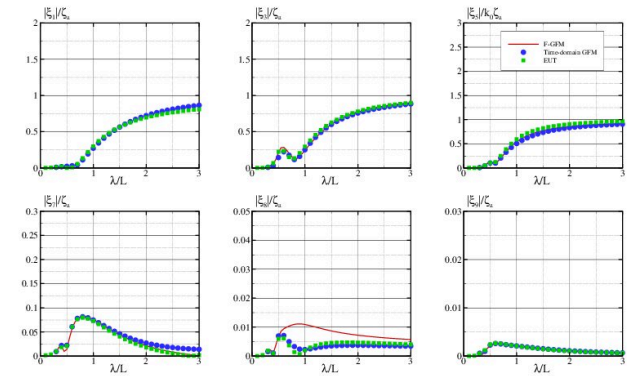Fig. 2 Wave exciting forces for elastic modes, Fn=0.0.

Fig. 3 Ship motion amplitudes in rigid and elastic modes.

5. Conclusions

In this research, the hydroelastic forces and the elastic deformation of a ship are computed by using the enhanced unified theory (EUT) combined with the modal superposition method for representing the elastic deformation of a body, and the normal velocity on the body surface due to elastic deformation is computed from the mode functions obtained by the uniform-beam approximation for a ship.

Through the comparison between EUT, Green-function method and Rankine panel method, it was confirmed that the results by EUT can provide reasonable accuracy and agreement and hence can be a practical tool. By using EUT, plenty of time could be saved due to very fast computation while enough accuracy still can be kept.

References
1) Bishop. R.E.D. and Price. W.G.: *Hydroelasticity of Ships*, Cambridge University Press, 1979
2) Kashiwagi, M.: Transactions of West-Japan Society of Naval Architects, No.89, pp.77-89, 1995
3) Newman. J.N.: Applied Ocean Research, Vol. 16, pp. 47-59, 1994.

Ultimate Strength of a Continuous Stiffened Panel under Combined Transverse Thrust and Inplane Shear

Aung Kyaw Htet

Ship Structural Integrity Subarea, Dept. of Naval Architecture and Ocean Engineering

***Key Words**: Stiffened panel, Ultimate strength, Buckling, Transverse thrust, Shear*

1. Introduction

A ship structure basically consists of thin plates on which a number of stiffeners are provided to increase their strength and stiffness. The side shell plating of bulk carrier, Fig.1, is subjected to the thrust in the shorter edge direction due to horizontal hull girder bending, and to the in-plane shear due to torsional moment. It has been recognized that larger plate and side-frame scantlings are required for the side shell plating ever since the strength requirements for the horizontal bending and torsional moment were introduced to the Common Structural Rule for Bulk-Carrier and Oil-Taker (CSR-BC&OT) issued by IACS (International Association of Classification Societies) in 2006.
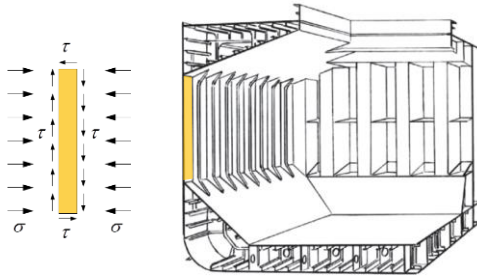
Fig. 1 Side shell plating of Bulk Carrier under combined loads.

In this study, the buckling/ultimate strength of a continuous stiffened panel subjected to combined transverse thrust and in-plane shear is investigated using nonlinear FEM. To consider the effect of continuity of the plating, the periodic boundary condition developed in the laboratory is used. The background of the plate-capacity and stiffener-capacity formulas given in the IACS/CSR is clarified. The simplified ultimate-strength formula developed by Fujikubo et al (OU formula)[1] is also considered. The ultimate strength is compared between FEM and the CSR and OU formulas and applicability of the formulas are examined.

2. FEM Collapse Analysis

When buckling/plastic collapse analysis is performed on a continuous stiffened panel, the minimum required region that can account for all possible bucking modes of plate and stiffener should be properly selected using relevant boundary conditions. Here we employ the periodic boundary conditions as shown in Fig. 2. When the rectangular plate of length a and width b is analyzed, the region $2a$ x $2b$ including two stiffeners is taken as a model for analysis. The condition that all displacements are same at the longitudinal edges AD and BC, and also at the transverse edges AB and DC, is imposed, assuming the same out-of-plane deformation is exerted periodically. This periodic boundary condition allows the buckling mode of either even or odd number of half waves to take place.

With regard to the in-plane displacements, all edges are assumed to be straight during whole collapse process considering interaction of adjacent panels. The periodic boundary condition is imposed on the in-plane displacements along the edges. In the previous studies of buckling behavior under in-plane shear, uniformly distributed shear stresses have been assumed. But in the proposed model, the shear stress distribution can change along the edges as the buckling deformation develops. This enables us to simulate the capacity reduction after shear buckling. The two representative nodal displacement U_R and V_R are defined at the corner node A. The transverse thrust is applied by V_R and the in-plane shear by U_R. Combined thrust and shear can be applied under any stress ratio and in either load or displacement control.
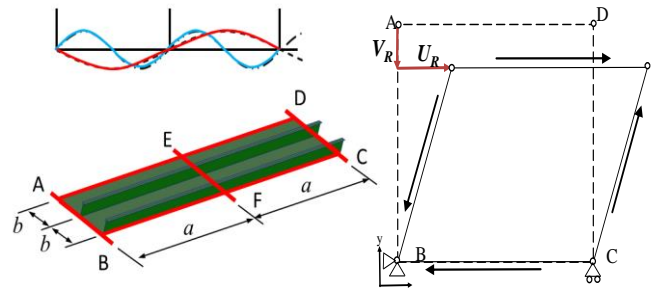

Fig. 2 Model for analysis using periodic boundary condition.

The initial deflection of local buckling mode is expressed as

$$w_o = \sum_{i=0}^{m} A_0 \sin\frac{i\pi x}{a} \sin\frac{\pi y}{b} + A_0 f_s(x, y) \qquad (1)$$

where the first term is the buckling mode under thrust and the second term the buckling mode under in-plane shear. The latter mode is calculated by FEM analysis. The initial deflection of stiffener is expressed by the tripping modes and the flexural mode as

$$v_o = C_o \frac{z}{h_s} \sin(\frac{\pi x}{a}) \quad , \quad w_{oall} = B_o \sin(\frac{\pi x}{a}) \qquad (2)$$

where $B_o = C_o = 0.001 \times a$. The amplitude A_0 is determined so that the maximum initial deflection is equal to the specified value. The dimensions and material properties are summarized in Table 1.

Table 1 Dimensions and material properties.

Plate width (b)	800 mm
Aspect ratio (a/b)	2, 4, 6
Plate thickness (t_p)	9, 16, 22, 28 mm
Angle-bar stiffener	$h \times b_f \times t_w / t_f = 300 \times 90 \times 10/16$
Young's modulus (E)	205,800 MPa
Poisson's ratio	0.3
Yield stress (σ_Y)	313.6MPa

3. Simplified Ultimate Strength Formula

3.1 CSR formula

In the CSR, the plate capacity, σ_{up}, and the stiffener capacity, σ_{us}, are calculated by different formulas, and the ultimate strength of a stiffened panel is determined by the smaller value of σ_{up} and σ_{us}. The plate capacity, σ_{up}, is given by the plastic correction of the elastic buckling strength of a bare plate. The stiffener capacity, σ_{us}, under the action of transverse thrust and in-plane shear is calculated by a concept of an equivalent lateral loads as follows:

(a)   (b)
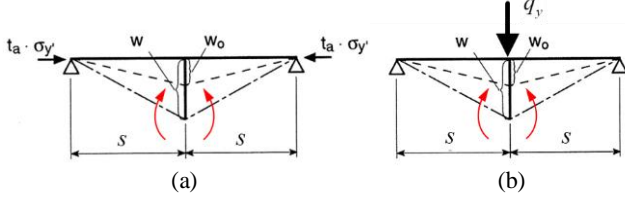
Fig. 3 Equivalent lateral load concept in CSR-BC&OT.

For instance, when transverse thrust acts, transverse bending moment is exerted as shown in Fig. 3(a). The equivalent lateral load q_y in the Fig. 3(b) is defined as a load per unit length that causes the same transverse bending moment. The stiffener capacity is evaluated by the longitudinal bending stress of the stiffener caused by the q_y distributing along the stiffener span. The applicability of this strength model is examined through the comparison of the collapse mode and strength with the FEM results.

3.2 OU formula

Fujikubo et al[1] derived the ultimate strength formula of a continuous unstiffened panel under transverse thrust as

$$\frac{\sigma_u}{\sigma_y} = \frac{b}{a}\left(\frac{2.4}{\beta} - \frac{1.4}{\beta^2}\right) + \left(1 - \frac{b}{a}\right)\left(\frac{0.06}{\beta} + \frac{0.6}{\beta^2}\right) \quad (3)$$

where β is the slenderness parameter given by

$$\beta = \frac{b}{t}\sqrt{\frac{\sigma_y}{E}} \quad (4)$$

The parameter β has a physical meaning of a square root of the yield strength to elastic buckling strength ratio. In the stiffened panel, the elastic buckling strength of local plate is increased by the torsional stiffness of stiffener. Using the increasing rate κ_y, derived analytically[1], the equivalent slenderness ratio with the effect of stiffener β_s is defined as

$$\beta_s = \frac{b}{t}\sqrt{\frac{\sigma_y}{\kappa_s E}} \quad (5)$$

Substituting the β_s into Eq. (3) instead of β, the ultimate strength of stiffened panel under transverse thrust is calculated.

4. Result and Discussion

The ultimate strength of stiffened panel obtained by FEM is compared with that predicted by the CSR and OU formulas. Fig. 4 shows the ultimate strength interaction curve obtained for the plate with the aspect ratio of 6. Fig.5 shows the deflection mode at the Post-ultimate behaviour for two calculation cases.

According to the FEM, the buckling collapse occurs in the local plate bucking mode under combined transverse thrust and

in-plane shear. The stiffener failure, as assumed in the CSR formula, has not been observed for the stiffened panels under consideration. As shown in Fig. 4, the OU formula gives good agreement with the FEM results slightly on the safe side. On the other hand, the CSR formula gives reasonable estimate when the in-plane shear is dominating, but it becomes over-conservative when the transverse thrust is dominating especially for large aspect ratio and large plate thickness. This is because the stiffener capacity equation gives smaller capacity than the plate capacity as the aspect ratio, and hence the span increases. Such stiffener failure is unreasonable referring to the FEM results. Some improvement is needed for the CSR formula. Although the results are omitted due to page limitation, the OU formula has also a room for improvement especially for very thin plate.
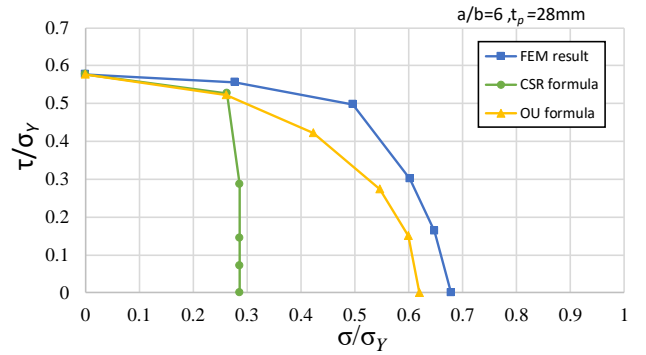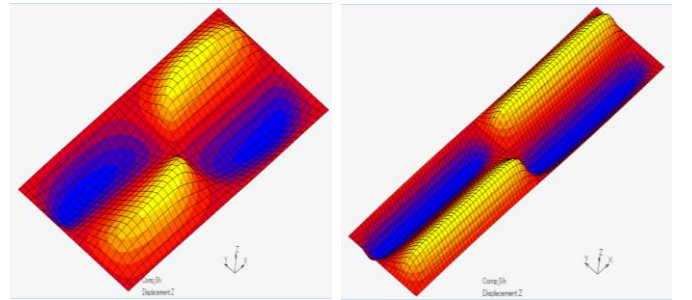

Fig. 4 Ultimate Strength interaction relationship of continuous stiffened panels under combined transverse and shear.

(a) a/b=2; t_p=16mm; σ:τ=1:2   (b) a/b=4; tp=16mm; σ:τ=1:0
Fig. 5 Buckling deformation under combined transverse and shear

5. Conclusions

For larger aspect ratio, especially for thicker plate, the ultimate strength obtained by CSR formula is remarkably lower than that of FEM results. This appears due to improper concept of equivalent lateral loads. This error may significantly influence the design scantling of the side shell plating of Bulk Carrier.

OU formula considering the effect of the stiffener gives reasonable estimate of the ultimate strength. But for the strength assessment of very thin plate, such as severely corroded plate, improvement should be made. This remains as a future work.

Reference

1) Fujikubo, M., Yao, T., Mohammad R K, Harada, M., and Yanagihara, D.: Estimation of Ultimate Strength of Continuous Stiffened Panel under Combined Transverse Thrust and Lateral Pressure Part2: Continuous Stiffened Panel, Marine Structure, pp411-427, 2005.

Adaptive Mitigation Approach for Tsunami Ascending to Meandering River

Rajuli Amra

Coastal Engineering Laboratory, Department of Civil Engineering

Key Words: *Intruding tsunami, meandering river, adaptive mitigation*

1. Introduction

Previous tsunami disasters revealed that tsunami could penetrate up far upstream of the river. It brought serious damage to river structures and flooded the residential area[1]. Tsunami propagating river exhibited very different actions from those observed on an open coast. Unfortunately, the existing tsunami protections were less effective in mitigating this typical tsunami [1].

Previous research highlighted that morphological features, tide and river discharge were some dominant factors in influencing propagation behavior [1][2]. However, the effect of river planform were not significantly addressed, although some research noted that the meandering part of the river might play the significant role[1]. Therefore, this study focuses on investigating the role of river geometry to tsunami characteristic. This research also proposes the new mitigation approach with respect to propagation behaviors and limitation of existing protection concept.

The proposed mitigation approach carried the concept of "extra room for the river". The result showed that the new approach was effective in countering the overflow, attenuating the wave height distribution along river, delaying tsunami arrival and reducing the capital cost.

2. Methodology

2.1 Scope and limitations

The investigation was conducted numerically by using 2D shallow water equation of COMCOT model, in which the tsunami was generated by 1m, 2m and 3m amplitude of solitary wave[3]. In order to clearly understand the effect of river planform, then the influence of other components, *e.g. river discharge, tide and morphological features*, were not considered. The sediment transport process was also not discussed. In addition, to isolate the overland flow from the shore, the very high wall was established and the wall structures both at the river banks and the shore were assumed stiff.

The tsunami behaviors were addressed by analyzing the maximum tsunami attributes, *i.e. wave height and resultant velocity,* along and lateral-river, tsunami arrival, overflow patterns and range of inundation. After that, the comparison was drawn between the two conditions, before and after proposed mitigation approach was applied.

2.2 River planform

Sine-generated curve function was employed in modelling symmetric meandering geometry, while the river bed elevation was modelled by empirical function of the transverse bed. Three planforms configuration were used for 10 km river-length to represent the complexity of natural river, which are low ($\theta_0=30^0$), moderate ($\theta_0=60^0$) and high-sinuosity meandering planform ($\theta_0=90^0$).

$$\theta(s) = \theta_0 \cos\left(2\pi s/L\right) \quad (1)$$

$$x(s) = \int_0^s \cos\left(\theta(t)\right)dt \quad (2)$$

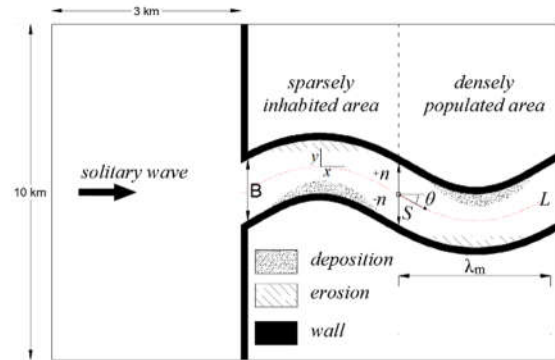$$y(s) = \int_0^s \sin\left(\theta(t)\right)dt \quad (3)$$

Fig. 1 Sketch of simulation area and notation for equations

2.3 Simulation Scenario

To understand the propagation behavior, three scenarios were set which were CS1, CS2 and CMS. Both CS2 and CMS scenarios were also used for investigating the effectivity of proposed mitigation approach, along with PM1 and PM2 scenarios. Each of cases was simulated for 60 minutes condition. The observation points were stationed per 1 km along river and each 20 m lateral-river at the bend apex. The river slope was assumed flat with 10 km length and 400 m width.

Table 1 Simulation Scenario

No	Scen.	Description
1	CS1	No river embankment installed
2	CS2	River wall height: 1.5 m uniform
3	CMS	River wall height: max. wave height of CS2
4	PM1	River wall height: varied along river
5	PM2	PM1 combined with "extra room" concept

3. Result and Discussion

3.1 Propagation characteristics

The simulation results described that the tsunami height along river exponentially decreased to the upstream distance. This pattern was qualitatively similar to all meandering level, even though there were a slight difference particularly at the inflection point. In addition, propagated wave height comparison among low, moderate and high-sinuosity planform also showed a small difference. For 1m, 2m and 3m initial tsunami wave height, it was known that the moderate-sinuosity planform dissipated tsunami better, compared to two other planforms. Yet, the difference was only by about 2%. The wave transmission ratio were correlated

well with the preserved energy. For 1m initial tsunami case, when overflow was not occurred, wave transmission ratio for all sinuosity level at the most upstream point was bigger than 85%, while it was only about 20% when overflow occurred. Surprisingly, the dissipation rate at the most upstream point increased significantly for case 2m and 3m initial tsunami height.

At the bend apex, the lateral distribution of tsunami height matched the previous study finding, in which the wave height at the outer bank tended to be higher, compared to the inner bank. In the contrary, the higher velocity distributions were at the inner bank. The interesting patterns were found at the case of 2m and 3m initial wave height for no overflow condition, in which the maximum lateral velocity distribution indicated the flow separation might occurred at the bend apex.

3.2 Overflow and inundation pattern

The overflow pattern was depended on the initial tsunami amplitude and correlated well with propagation characteristics, in which the propagating tsunami tended to easily overtop the embankment at the downstream river, as shown in Fig. 2. The CS2 results showed that the northern part of the river were inundated greater, while longest overflow occurred at the southern part of the river.

The result also described that the higher inundation were more dominant at the concave banks. For high sinuosity planform, this behavior was more significant, compared to other two other planform. This pattern might relate to centrifugal force that applied in curved path.
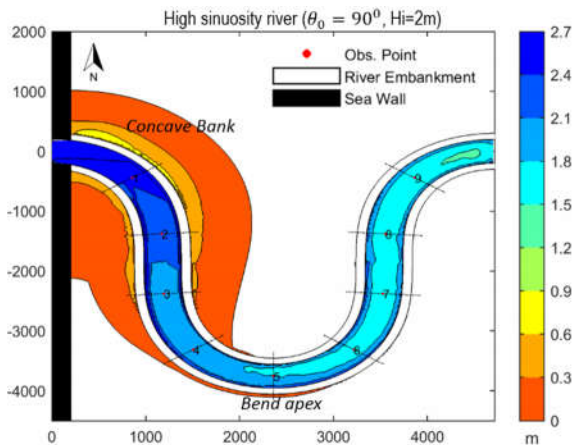

Fig. 2 Sample of overflow distribution for CS2 scenarios

3.3 Effectivity of proposed mitigation approach

Elevating the river embankment as CMS scenario proved effective in countering the overflow along the river. However, preserving the propagated wave in the river caused the increasing of wave height in the river. The increasing wave height followed by the velocity and ultimately raised the force distribution. It could endanger the in-river structure, e.g. bridge and jetty, and indeed the river embankment itself, particularly at concave banks. The elevated wall also accelerated tsunami arrival time at the most upstream point. The typical characteristic applied to all sinuosity level of the river.

For the case of 2m initial tsunami height, raising the embankment from 1.5m to 3.25m uniformly along river boosted the initial cost about 117%. The cost could be reduced if the embankment was elevated gradually along the river, based on maximum wave height distribution. This method only increased

about 57% of the initial construction cost. Still, both uniformly or gradually elevated wall will increase the wave height at the most upstream point and decrease dissipation rate by 5%. Indeed, for PM1 scenario, the small part of area that was classified as densely inhabited zone was inundated.

Another alternative was increasing the river capacity by relocating the embankment at the downstream river. In the PM2 scenario, both side of embankment up to 1.5 river km, which cross-sectional to the centerline, was relocated about 350m away to create 100ha "extra room". Combination of "extra room" concept and gradual embankment positively decreased wave distribution in the river, compared to previously mentioned approaches. As shown in Fig.3, the most drastic wave reduction was at 1km point from the river mouth, in which the wave height has decreased by about 40%. While it was only about 20%, 10% and 9% for CS2, CM and PM1 cases consecutively. The arrival time of tsunami at the most upstream point was also decelerated. In addition, the riverside area was not inundated.
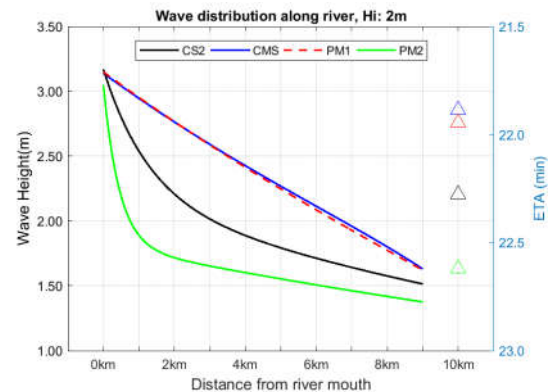

Fig. 3 Comparison on wave height and arrival time for θ_0=60^0, lines indicated wave height, markers showed arrival time

Several variation of PM2 scenario revealed that the effectivity of the proposed concept was constrained by "extra room" capacity, enlargement orientation, i.e. lateral or along river expanding, and the starting point of river embankment relocation. Since the propagation behavior was, *almost*, similar in all sinuosity level, then the proposed concept is assumed applicable to any meandering river planform.

4. Conclusions

Generally, it could be concluded that different meandering level of river respond in similar mechanism to the intruding tsunami wave. However, the higher sinuosity planform tends to be inundated greater at the bend apex section. In addition, propagation patterns tends to follow the river shape. Finally, the proposed mitigation concept proved more effective in attenuating wave height distribution and decelerating tsunami arrival time.

References

1) Tanaka H: Study on the relation of river morphology and tsunami propagation in rivers, Ocean Dynamic, Springer, 2014.
2) Elena T: Tsunami Penetration in Tidal Rivers, with Observations of the Chile 2015 Tsunami in Rivers in Japan, Pure and Applied Geophysics, 2016.
3) Philip L.F. Liu, Harry Yeh and Synolakis C: Advanced Numerical Models for Simulating Tsunami Waves and Runup, W Scientific, 2008.

S-PIV (Stereo-Particle Image Velocimetry) Measurement for a Self-propelled Ship in Regular Head Waves with Different Amplitudes

Mwangi Benson Oyunge

Hull Form Design Sub-area, Department of Naval Architecture and Ocean Engineering

Key Words: *KVLCC2, EFD, Particle Image Velocimetry, Flow Field Measurement, Wave Amplitude Dependency*

1. Introduction

The self-propulsion performance in regular head waves of KVLCC2 model including ship motion were investigated by Wu et al[1]. The CFD computation results were compared with experiment. The CFD could predict the detailed thrust fluctuation in one period including higher harmonics. But the computation and experiments were done for only one wave height. The flow field around self-propelled ship model including nominal velocity field for without propeller condition were measured and compared with CFD computation. In the Study of Wu, the relation between thrust time history and flow field were discussed and the vertical relative motion between propeller disk and the bilge vortices are very important to explain the thrust fluctuation.

So, it seems that the wave amplitude has a lot of effect on thrust fluctuation and averaged wake. In this study, the flow field around stern is measured using the SPIV as well as thrust, torque, towing force and 3DOF motion to investigate how the velocity distribution changes with the wave amplitude and its effect on the amount of thrust delivered by the propeller.

2. Experiment Overview and Test Conditions

2.1 Experiment Overview

The experiments were conducted at the Osaka University towing tank using a fully-loaded 3.2m KVLCC2 tanker model in long regular head waves with different wave amplitudes at a design Froude number, Fr=0.142 (0.795m/s). The motions and force measurement experiment was done first for with and without propeller condition while PIV experiment was done later for without propeller condition. The flow field at AP section was measured because the laser reflection effect was large for propeller plane and the flow field is similar as propeller plane to consider the thrust fluctuation from boundary layer assumption. For the self-propulsion experiment, 4 blades, 0.986m diameter MOERI propeller model was used. The ship model particulars are as shown in Table1 and Fig.1 shows the ship model and the coordinate system used in this experiment. The propeller model used is as shown in Fig 2.

Fig. 1 KVLCC2 Tanker model and coordinate System.

Fig. 2 MOERI Propeller model.

2.2 Test Conditions

For this experiment, three waves of λ/L=1.1, 1.6 and 2.0 were chosen because the large relative motion between propeller disk and low velocity region due to bilge vortices was observed in previous study for long waves. Various wave amplitudes i.e. A=0.75, 1.5, 3, 4, 4.3cm were used for each wavelength. Ship motion in this experiment is 3DOF (degree of freedom) in which the ship was free to heave, pitch and surge. These motions were measured by potentiometers. In self-propulsion experiment, thrust and torque were measured by a motor-driven dynamometer connected to the propeller by a shaft. Force in x-direction was measured by a dynamometer which was attached to the heaving rod. The incident wave data was measured at the wave gauge that was installed 3.52m (1st experiment) and 3.314m (2nd experiment) upstream of FP.

The flow field at AP was measured by the S-PIV system for the same conditions as above. For larger wave amplitudes the PIV measurement was done in two vertical positions with an overlap

Table 1 KVLCC2 Tanker model particulars.

Ship Length	L_{PP}(m)	3.2
Breadth	B(m)	0.58
Depth	D(m)	0.3
Draft	d(m)	0.208
Vertical Center of Gravity	KG(m)	0.186
Displacement	∇(m^3)	0.313
Moment of Inertia	K_{YY}/L_{BP}	0.247
Block coefficient	C_B	0.8098
Longitudinal Center of Buoyancy	LCB (%LPP) fwd+	3.48

so as to capture the whole flow field. The average number of images collected per phase is 180 so as to get sufficient data for image analyses to get the phase averaged flow field.

3. Results and Analysis

The motions and force measurement results were analyzed by Fourier series expansion and the data was reconstructed by ignoring the higher harmonic than 7th harmonic to understand the fluctuation shape in one period. So, for thrust and torque a lot of noise due to vibration of connection joint between motor and self-propulsion dynamometer was eliminated. It was noted that the 1st, 2nd and 3rd harmonic components are responsible for the thrust oscillations with a quickly increasing upward slope and a slowly decreasing downward slope. Similar observation was made by Emel et al[2] with a conclusion that the cause could be the relative motions between bilge vortices and ship motions and pressure gradient between inner and outer boundary layers.

From the Fourier analysis, the harmonic components responsible for the original trends of motions and forces were determined. For motions, it was found that 1st harmonics is enough to achieve the original motion trend whereas for thrust and torque we need up to 3rd harmonic components. From the heave time history in Fig. 3, its amplitudes of oscillation increases with increase in wave amplitude and Fig. 4 shows that the 1st harmonic amplitudes of heave increase linearly with wave amplitude. The same trends are shown by pitch motion.
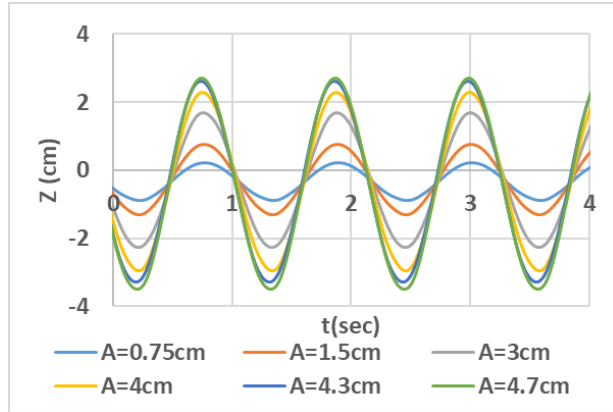

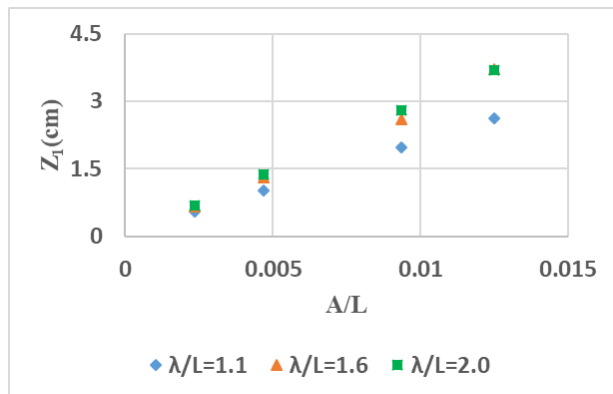Fig. 3 Heave time history for wave peak at propeller plane.

Fig. 4 Heave 1st Harmonic amplitudes.

Fig. 5 shows that mean thrust decreases slightly with increase in

wave amplitude whereas the inflow velocity into the propeller plane increases with increase in wave amplitude as shown in Fig. 6.
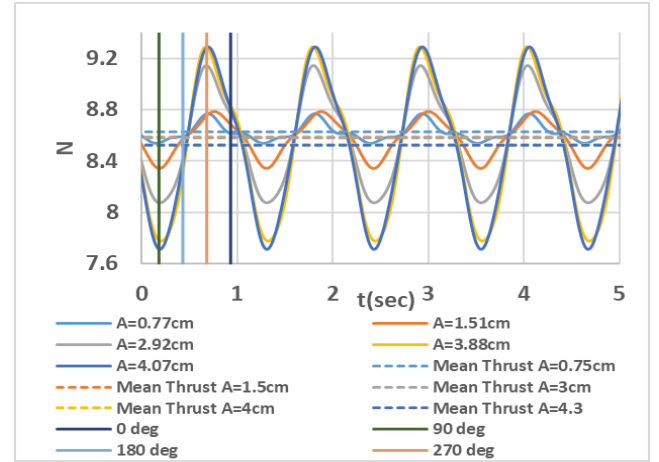

Fig. 5 Thrust time history with mean values in λ/L=1.1 for different wave amplitudes.
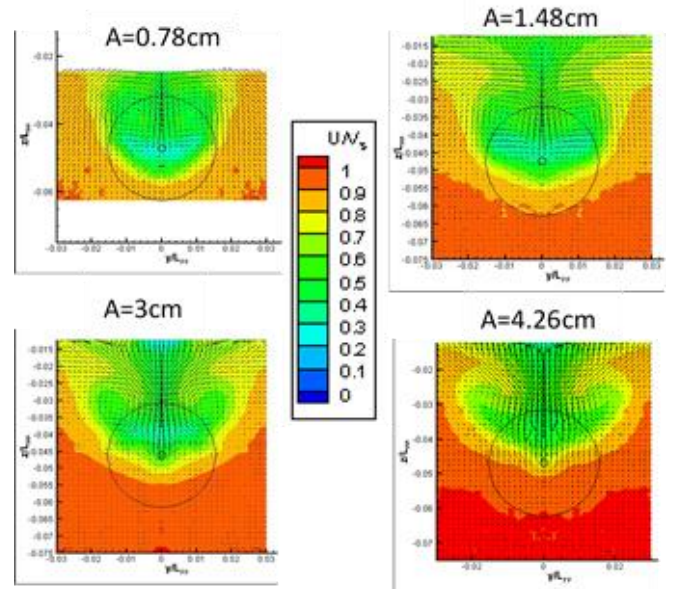

Fig. 6 Velocity distribution for phase 90 at AP for different wave amplitudes.

4. Conclusions

The velocity distribution at AP was analyzed and discussed with respect to the thrust fluctuation in waves. The trend can be explained although the velocity field was measured for without propeller condition. The motions and thrust time histories in waves of different amplitudes were computed by CFD and the CFD results show fairly good prediction as in the presentation.

References

1）Ping-Chen et al: Proc. of 30th Symposium on Naval Hydrodynamics (Tasmania, Australia), 2014
2）Emel et al: JASNAOE, pp.255-258,2015

Verification & Validation of a Cellular Automaton Simulating Under-Film Corrosion

Ivan Kristov,
Ocean Material Engineering Laboratory,
Department of Naval Architecture & Ocean Engineering.

Key Words: *Under-Film Corrosion, Random Fields, Cellular Automaton, Verification & Validation process, Covariance Structure*

1. Introduction

To understand the influences that under-film corrosion has on metal selection is currently insufficient in providing adequate performance predictions for new Corrosion Resistance Steels (CRSs), without long-term experiments. There a few methods that can model the incubation and extension of epoxy coating failures. This has prompted the need for a 2D cellular automaton (CA) is based on a modified version of IACS CSR-H's 3-phases probabilistic model.

As part of the CA development, the model needs to undergo a Verification and Validation process (V&V) consisting of a sensitivity analysis on cell size and optimization examination on the number of internal runs for a simulation. From these modifications, a re-examination will be performed on the results of a single scribe defect reported by Osawa et al [1]; and the double scribe defect reported by Oda et al [2].

2. Verification and Validation process

The purpose of this V&V is to improve the accuracy of the CA while maintaining (or improving) the simulations run-time. This will be achieved through two methods: the evaluation of the results acceptable error based on the number of runs within the simulation; and the influence that cell size has to the CA.

2.1 Optimization study of Internal Computational Runs Per-Simulation

The confidence interval formula, equation (1), shown below is used to determine the balance between accuracy and the number of runs for the CA.

$$x_{bar} = \pm z \frac{s}{\sqrt{n}} \qquad (1)$$

where, x_{bar} is the sample mean, z is the confidence level set to 99% (= 2.575), and s is the standard deviation and n is the size of the sample. This equation is used to measure the standard error of 10 simulations with changing number of internal runs (n) for each averaged cell position value over 10 simulations (s) that forms the uniformed surface profiles (corroding valley).
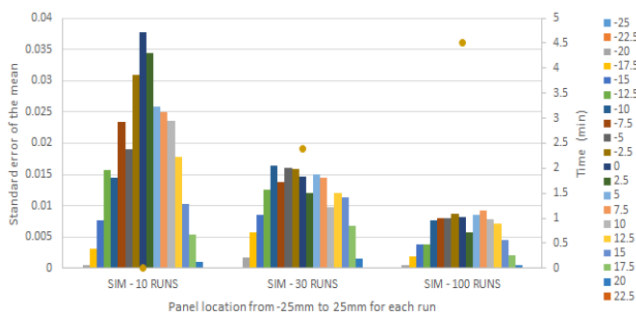

Fig 1. Standard error for each cell position for simulations with 10, 30, and 100 internal runs against processing time.

Fig 1 shows the original 10-run simulation against 30 and 100 internal runs for the maximum error vs each cell position from -25mm to 25mm. The graph also shows the duration for each simulation indicating that 30 internal runs provides the best reduction of overall error within an acceptable processing time.

2.2 Cell Size Sensitivity Analysis

After a lengthy investigation, a correlation was proposed that the probability of a pit occurring within the cell ($Ppit$) was influencing the depth. As the area of a cell was reduced/increased by changing the cell size, $Ppit$ was unchanged resulting in a higher probability of a pit occurring in the same area. This would cause an earlier initiation of a pit within a cell resulting in a deeper pit due to a longer duration. This relationship is shown in equation (2),

$$\frac{c_{org}}{c_{new}} = \sqrt{\frac{P_{pit_{org}}}{P_{pit_{new}}}} \qquad (2)$$

where, C_{org} is the original cell size, C_{new} is the new cell size. $Ppit_{org}$ is the original probability of a pit occurring in the cell and $Ppit_{new}$ is the new probability of a pit occurring in the cell.

Results for both CRS and conventional steel where compared with the original 2.5mm CA for 5mm, 1.25mm and 0.625mm. Fig 2 shows the original simulations with 2.5mm cell size and the original $Ppit$ of 0.036 for both CRS and conventional steel. The figure also includes the new simulations with a cell size of 1.25mm and new $Ppit$ of 0.009 for comparison. All simulations are presented with a minimum and maximum error profile.
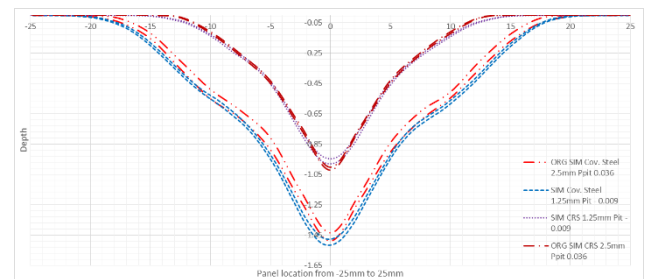

Fig 2. The original CRS and convention steel simulations compared against new simulations with changed $Ppit$ (0.0009) and cell size (1.25mm).

Fig 2 confirms that changing Ppit will allow the CA to be scaled. However, there is an increase in divergence when the cell size is reduced further to 0.625mm from 2.5mm, which may be caused by the cellular automaton neighbor rules, e.g. coating life and coating degradation, which controls the corroding valley's slope.

3. Re-examination of Scenarios from Previous Work

From the V & V, a re-examination is now required of past work to ensure that the simulations produced by the CA are the best depiction of the experiments possible.

This will only require slight changes to a select number of input parameters. This investigation will repeat the process in simulating both the single and double scribed analysis reported by Osawa et al [1] and Oda et al [2].

3.1 Re-examination of Single Scribe Defect [1]

The V & V found that the results of the CA had maintained an accurate correlation with the experiments blister width for a 1.25mm cell size simulation. However, the depth and inclination of the corroding valley could be improved upon. This was achieved by repeating the simulation refinement process presented in reference [1] from step 3 by decreasing the percentage of the mean and standard deviation of a, which controls the depth of the corroding valley. Followed by step 4 in altering the following parameter A_s, which controls the slope of the corroding valley.
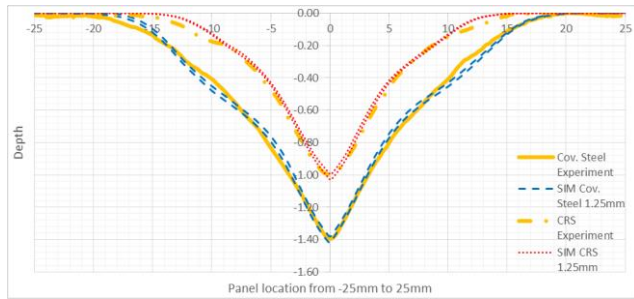

Fig3. 2D corrosion wastage profiles comparison of CRS and conventional steel experiments against simulation created by the CA.

These results have indicated that the accuracy of a CA's simulation can be improved upon by changing the scale of the model's geometry with only slight corrections required of key parameters, a and A_s. With Conversional steel decreasing only a by 85% and a and A_s for CRS by 65%. With only A_s requiring attention when simulating corrosion wastage of CRS as the shielding effect has a larger influence to the mathematical model then when modeling conventional steel.

3.2 Re-examination of double scribe defect [2]

The double scribe simulation begins by defining the input parameters from a single scribe experiment, which are then used in the double scribe simulations. This methodology is used to allow more complex scenarios to be simulated once the coating and metal's physical characteristics have been defined from the simpler scenario under the same environmental conditions.

The conditions changed for this re-examination of the single scribe defect from reference [2] was the cell size (1.25mm) and only a and A_0, by 65%. However, the corroding valley for this experiment showed two slopes create by increased corrosion from 15mm the scribe. The previous examination took the average but for this examination, the inner slope is selected. These parameters were then used for the double scribe defect simulation, which concurred with previous results showing symmetry.

The generation of Random Fields for a and A_0 was repeated with a range of 20mm to provide covariance structure for these parameters, with the results shown in Fig 4.
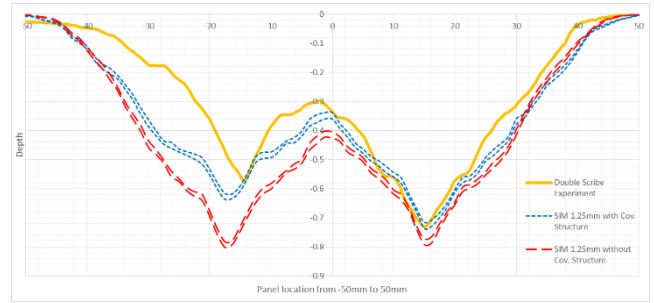

Fig4. Double scribe defect simulations with and without covariance structure for a and A_0.

The probability of occurrence was then re-examined with minor alterations to the methodology in reference [2]. The method starts with quantifying the relationship between the two corroding valleys' depths to a single entity (α), which is achieved with equation [2],

$$\alpha = \frac{|L_{max}| - |R_{max}|}{|d_{avg}|} \quad [2]$$

where, L_{max} and R_{max} are the maximum depth of the left half and right half of the averaged surface profile, and d_{avg} is the average of L_{max} and R_{max}.

The statistical population data of α is generated by the CA of one internal run per 1000 simulations, which differed, to the original ten runs per 300 simulations. Table 3 shows the percentage of probability of occurrence for the CA against each experiment including their average. The results presented have confirmed the need for using random fields to provide certain parameters in the CA with covariance structure to resolve the non-symmetry found in corrosion.

Table 1. Comparison of the probability of occurrence for α with and without covariance structure.

Case	No Covariance structure included	Covariance structure included
Experiment 1	4.37%	21.63%
Experiment 2	0.47%	11.18%
Experiment 3	0.02%	5.09%
Experiment Avg.	0.62%	12.07%

4. Conclusions

The V&V process has meet its objectives of providing a method to refine the CA's accuracy against a scenario and allowing the CA to be scalable. This has been confirmed from the re-examination process showing improvements in simulating both scenarios.

5. References

1) Osawa, et al (2016) "Development of Under-Film Corrosion Simulation Method based on Cellular Automaton", Proc.OMAE2016,paper OMAE2016-54508.
2) Oda, et al (2018) "Study on Under-Film Corrosion Simulation Considering Covariance Structure of the Random Parameters",Proc.JSNAOE2018, paper JASNAOE2018-0323.